Nonlinear Processes in Geophysics (1995) 2: 241 - 268

Nonlinear Processes in Geophysics

Successive bifurcations in a shallow-water model applied to the wind-driven ocean circulation

S. Speich[1,2], H. Dijkstra[3] and M. Ghil[1,4]

[1] Dept. of Atmospheric Sci., Inst. of Geophys. and Planetary Physics, Univ. of California, Los Angeles, CA 90095-1565, USA
[2] Present address: Lab. d'Océanographie Dynamique et de Climatologie, Univ. P. et M. Curie, 75252 Paris Cedex 05, France
[3] Inst. for Marine and Atmospheric Research, Univ. of Utrecht, Princetonplein 5, 3584 CC Utrecht, The Netherlands
[4] Sabbatical address: Département Terre-Atmosphère-Océan, Ecole Normale Supérieure, 75231 Paris Cedex 05, France

Received 20 November 1994 - Accepted 14 August 1995 - Communicated by D. Sornette

Abstract. Climate – the "coarse-gridded" state of the coupled ocean-atmosphere system – varies on many time and space scales. The challenge is to relate such variations to specific mechanisms and to produce verifiable quantitative explanations. In this paper, we study the oceanic component of the climate system and, in particular, the different circulation regimes of the mid-latitude wind-driven ocean on the interannual time scale. These circulations are dominated by two counterrotating, basin-scale gyres: subtropical and subpolar.

Numerical techniques of bifurcation theory are used to study the multiplicity and stability of the steady-state solutions of a wind-driven, double-gyre, reduced-gravity, shallow-water model. Branches of stationary solutions and their linear stability are calculated systematically as parameters are varied. This is one of the first geophysical studies in which such techniques are applied to a dynamical system with tens of thousands of degrees of freedom..

Multiple stationary solutions obtain as a result of nonlinear interactions between the two main recirculating cells (cyclonic and anticyclonic) of the large-scale double-gyre flow. These equilibria appear for realistic values of the forcing and dissipation parameters. They undergo Hopf bifurcation and transition to aperiodic solutions eventually occurs. The periodic and chaotic behavior is probably related to an increased number of vorticity cells interacting with each other.

A preliminary comparison with observations of the Gulf Stream and Kuroshio Extensions suggests that the internal variability of our simulated mid-latitude ocean is an important factor in the observed interannual variability of these two current systems.

1 Introduction

Dynamical systems theory has been applied to climate variability on different time scales. The pioneering work of Budyko (1969), Sellers (1969), and North et al. (1981) has introduced multiple equilibria to the study of paleoclimatic variations. Intraseasonal variability of the atmosphere (e.g., Charney and DeVore, 1979; Legras and Ghil, 1985; Vautard and Legras, 1988; Strong et al., 1995), seasonal-to-interannual variability of the ocean-atmosphere system in the tropics, in particular the El Niño-Southern Oscillation (ENSO) phenomenon (e.g., Philander, 1990; Neelin et al., 1992; Jin et al. 1994), and interdecadal-to-millenial variability of the oceans' thermohaline circulation (Stommel, 1961; Bryan, 1986; Weaver et al., 1991; Thual and McWilliams, 1992; Quon and Ghil, 1995) have been studied by following successive bifurcations through limit cycles to strange attractors. This approach was motivated by the nonlinearities of the equations governing the atmosphere and oceans. The behavior of their solutions changes qualitatively only at isolated points in phase-parameter space, the bifurcation points. Behavior along a single branch of solutions, between such points, is modified only quantitatively and can be explored by linearization about the basic state which changes smoothly as parameters change (e.g., Ghil and Childress, 1987).

The truly nonlinear behavior near bifurcation points involves robust transitions, of great generality, between single and multiple equilibria (saddle-node, pitchfork and transcritical bifurcations), equilibria and limit cycles (Hopf bifurcation), and on to tori and strange attractors (Guckenheimer and Holmes, 1983). Chaos and strange attractors are not restricted to low-order systems (Constantin *et* al., 1989; Témam, 1988). The detailed exploration of finite- but high-dimensional attractors in climate dynamics has begun in the last decade (e.g., Legras and Ghil, 1985; Lorenz, 1990; Dijkstra and Neelin, 1995). The mathematical tools of dynamical system theory permit

Correspondence to: S. Speich

us to explore the system's phase-parameter space from the simplest, most symmetric states to highly complex and realistic ones, with much lower symmetry in space and time. The exploration can proceed in its first stages by analytical methods (e.g., North et al., 1981; Jin and Ghil, 1990) and more fully by numerical algorithms, such as pseudo-arclength continuation (Keller, 1977; Legras and Ghil, 1985; Dijkstra, 1992); the method we use systematically in the present study belongs to the latter.

Continuation methods enable one to follow efficiently a branch of steady-state solutions as a single parameter varies continuously, rather than merely computing trajectories of a particular system of equations for a large number of different parameter values. An additional advantage of these methods is that unstable steady states can also be computed; these might not be of direct physical relevance, but they do show how branches of stable steady states are connected and can influence the behavior of time-dependent solutions nearby (Ghil and Childress, 1987, Ch. 6). Continuation methods have been applied to atmospheric models with $O(10^2–10^3)$ discrete variables (e.g., Legras and Ghil, 1985; Keppenne, 1989). The work we present in this paper represents the first oceanographic study of a model with $O(10^4)$ variables, a number which starts approaching that of advanced general circulation models [$O(10^5–10^6)$]. The linear stability of a continuum of steady states is determined simultaneously by the present method; this feature is important, since it enables one to monitor the occurrence of limit cycles via Hopf bifurcation of the steady states.

Our aim here is to investigate the nonlinear behavior of a model of the double-gyre mid-latitude wind-driven circulation and the dependence of its flow regimes on the major physical parameters that control it. Numerical simulation of idealized single- and double-gyre ocean basins has been crucial in the study of nonlinear effects added to the classical Stommel and Munk models and of the dynamics of western boundary currents (WBCs), their separation from the coast and confluence in mid-latitude jets such as the Gulf Stream and the Kuroshio Extensions (e.g., Bryan, 1963; Robinson, 1983; Cessi et al., 1987; Le Provost and Verron, 1987; Ierley and Young, 1988; Cessi and Thompson, 1990; Verron and Jo, 1994). In our study, we emphasize multiple equilibria and low-frequency variations. Evidence of such variability is restricted by the paucity of oceanographic data for the major extratropical current systems. Still, a few observational studies do suggest interannual variability of the Kuroshio-Oyashio (Qiu and Joyce, 1992), the Gulf Stream-Polar Current (Auer, 1987; Brown and Evans, 1987; Levitus, 1990; Hanson, 1991), and the Brazil-Malvinas current systems (Olson *et* al., 1988). Theoretical studies of interannual variability, in particular that of the WBCs, have been rather limited and the mechanisms governing this variability are not fully understood so far (Ierley, 1990; McCalpin and Haidvogel, 1995).

Only recently has a dynamical-systems approach been brought to bear on the dynamics of WBCs (Jiang et al., 1995a; Cessi and Ierley, 1995). Multiple equilibria of the wind-driven, single-gyre quasi-geostrophic (QG) vorticity equation (Veronis 1966a; b) were studied by Cessi and Ierley (1995) using Newton's method rather than forward integrations. The picture resulting from their numerical work involves up to seven multiple steady states in a parameter space defined by the lateral viscosity and bottom friction. No oscillatory solutions for the QG model could be found by this method.

Jiang et al., 1995a (JJG hereafter) have obtained multiple equilibria, oscillatory and chaotic solutions of a wind-driven, primitive-equation (PE), reduced-gravity model, by computing model trajectories for a fairly large number of parameter values. They imposed a symmetric double-gyre zonal wind stress, constant in time, as used in many eddy-resolving, QG numerical simulations (e.g., Holland 1978). By repeated experiments with different wind-stress magnitudes and dissipation coefficients, they were able to construct approximate bifurcation and catastrophe diagrams depicting the dependence of the steady-state solutions on these two parameters. Multiple steady states, periodic and aperiodic solutions arise in succession as the wind forcing is increased. The multiple equilibria have a nearly antisymmetric structure with respect to the mid-basin axis where the wind-stress curl is zero, defined as the *R*-line. JJG showed the intrinsically nonlinear nature of the solutions so obtained. In their results, despite the symmetric wind forcing, the point of separation from the coast of the WBCs is found south or north of the *R*-line, as observed in the real ocean (e.g., Boland and Church, 1981; Olson et al., 1988).

The purpose of the present article is to provide a complete quantitative description of double-gyre, wind-driven mid-latitude ocean dynamics in a shallow-water, reduced-gravity model with simplified geometry forced by a constant zonal wind stress. The PE shallow-water formulation of JJG showed a wide spectrum of model responses to such a forcing, including nearly antisymmetric equilibria and internal ocean variability. For the classical QG approach, asymmetric solutions have been obtained more often by prescribing an asymmetry in the zonal wind stress (e.g., Moro 1990). So far, multiple equilibria only have been shown to exist for a barotropic QG model forced by an antisymmetric zonal wind pattern (Cessi and Ierley 1995), although Le Provost and Verron (1987) were able to obtain unstable barotropic flows for some values of their physical parameters in a double-gyre QG model, while McCalpin and Haidvogel (1995) obtained only chaotic solutions in theirs. Haidvogel et al. (1992) argue that higher-order, ageostrophic effects are important in WBC separation, while using basically a QG model. For reasons of continuity in our systematic exploration of internal ocean variability and nonlinear effects, we examined essentially the PE model of JJG, rather than attempting to select an intermediate balanced model (McWilliams et al.,

1990). The model choice is dictated ultimately by the competing requirements of relative simplicity and reasonable size, to permit the application of an advanced pseudo-arclength continuation code (Dijkstra, 1992), and of acceptable physical realism, to capture a significant subset of upper-ocean dynamics. The model is described in Section 2, and the pseudo-arclength methodology is presented succinctly in Section 3, with further details in an appendix.

In Section 4 we analyze the stationary solutions, and their dependence on some of the model's nondimensional parameters: the amplitude of the forcing, the Ekman number, the Rossby number, the nondimensional β parameter, and the bottom drag coefficient. We discuss how model solutions vary in number, stability and spatial features with the parameters. In Section 5, the nature of the oscillatory instabilities and the limit cycles they give rise to are investigated. In Section 6, transitions to aperiodic solutions is studied through the computation of specific trajectories. The dependence of this transition on the basin size is emphasized, along with a brief comparison to available ocean data.

A summary of the results follows in Section 7. Despite the model's simplicity, its behavior is relatively realistic in the solutions' spatial patterns and in the temporal variability of the oscillatory solutions. This suggests that the model, used here mostly for illustrative, methodological purposes, might still have some relevance to mid-latitude oceanic flows.

2 Model Formulation

We focus on the nonlinear behavior of the wind-driven circulation in a closed ocean basin whose dynamics is governed by reduced-gravity, shallow-water equations (JJG), forced by a double-gyre antisymmetric wind-stress pattern. The mid-latitude ocean is modeled as a single layer of fluid of constant density ρ and variable thickness $h(x, y, t)$, overlying a deep and motionless layer of density $\rho + \Delta\rho$. The model domain is confined to a rectangular basin given by $0 \le x \le L$ and $0 \le y \le D$. The equilibrium depth is fixed at H = 500 m, to have the model's (barotropic) Rossby-wave velocity close to the (first baroclinic) mode which is dominant in the mid-latitude oceans. Since all thermodynamic effects are neglected in the model, the interface between the two fluid layers is an isopycnal surface, thought of as the ocean's permanent thermocline (Pedlosky 1987).

The governing partial differential equations (PDEs) are:

$$\frac{\partial U}{\partial t} + \nabla\cdot(U\mathbf{v}) = -g'h\frac{\partial h}{\partial x} + fV + A\nabla^2 U - RU + \frac{\tau^x}{\rho}, \tag{2.1a}$$

$$\frac{\partial V}{\partial t} + \nabla\cdot(V\mathbf{v}) = -g'h\frac{\partial h}{\partial y} - fU + A\nabla^2 V - RV, \tag{2.1b}$$

$$\frac{\partial h}{\partial t} = -\frac{\partial U}{\partial x} - \frac{\partial V}{\partial y}, \tag{2.1c}$$

where

$$U\mathbf{i} + V\mathbf{j} = h\mathbf{v} = h(u\mathbf{i} + v\mathbf{j}) \tag{2.1d}$$

is the upper-layer mass-flux vector, while u and v represent, respectively, the eastward and northward components of the velocity in the upper layer, and h the upper-layer thickness; g' is the reduced gravity, $g' = g(\Delta\rho/\rho)$, with g the acceleration of gravity. We solve the equations on the beta-plane, i.e., $f = f_o + \beta_o y$.

The standard parameter values used here follow JJG, with L = 1000 km, D = 2000 km, $f_o = 5\cdot10^{-5}$ s^{-1}, ρ_o = 1022 kg m^{-3}, and g' = 0.031 m s^{-2}. The size of the domain to be investigated in detail has been dictated by the compromise between a marginally eddy-resolving grid of $\Delta x = \Delta y$ = 20 km and a total number of discrete variables that the continuation method can handle. A much larger domain, with L = 6400 km and D = 4400 km, is studied in section 6.2, where model results are compared to the observations.

The zonal wind stress, τ^x, forcing the ocean flow appears as a body force in Eq. (2.1a) and is constant in time and proportional to the standard sinusoidal pattern $-\tau_o cos(2\pi y/D)$ often used in such mechanistic studies (e.g., Holland and Lin, 1975); the proportionality factor, τ_o, is the amplitude of the wind. Horizontal eddy diffusion is represented by an harmonic operator with a coefficient A = 300 m^2 s^{-1}, while bottom friction is of Rayleigh-type and it is scaled by $R = 5\cdot10^{-8}$s^{-1}.

The normal flow is zero at the lateral boundaries, while the boundary conditions for the tangential velocity are expressed by the relations:

$$(1-\gamma)v + \gamma\frac{\partial v}{\partial x} = 0 \quad \text{at } x = 0, L, \tag{2.2a}$$

$$(1-\gamma)u + \gamma\frac{\partial u}{\partial y} = 0 \quad \text{at } y = 0, D, \tag{2.2b}$$

where the boundary viscosity parameter γ has the limiting values of 0 for no-slip boundary conditions and 1 for the free-slip ones. Here, we assumed no-slip boundary conditions. Sensitivity experiments to no-slip versus intermediate and free-slip boundary conditions were carried out by JJG, following Haidvogel et al. (1992). With intermediate and free-slip boundary conditions the model becomes more energetic but the essential flow structures are preserved. McCalpin and Haidvogel (1995) assumed free-slip and obtained more chaotic solutions for similar parameter values, in agreement with the results of JJG.

At the coast (the solid boundaries here) both velocity components vanish, so the no-slip boundary conditions are mathematically correct, but the boundary layers are

insufficiently resolved in this and similar models. Verron and Blayo (1995) showed sensitivity of Gulf Stream separation in the QG equations to different numerical implementations of the no-slip boundary conditions. This sensitivity appears to be similar to that noticed by Haidvogel et al. (1992) in their QG study of γ-dependence of solutions. Equally detailed studies of solution dependence on the numerical aspects of boundary conditions in a PE model like the present one are beyond the scope of the exploratory study at hand.

We introduce nondimensional variables by

$$x = Lx', \quad y = Ly', \quad (u,v) = U^*(u',v'), \quad t = \frac{L}{U^*}t',$$
$$h = Hh', \quad \tau = \tau_o \tau'. \tag{2.3}$$

The characteristic value of the velocity U^* is simply taken to be equal to 1 m s^{-1}, a reasonable magnitude for the velocity in a WBC. The system of equations (2.1) becomes:

$$\varepsilon\left[\frac{\partial U}{\partial t} + \nabla\cdot(U\mathbf{u})\right] =$$
$$-\varepsilon Fh\frac{\partial h}{\partial x} + (1+\varepsilon\beta y)V + E\nabla^2 U - \mu U + \sigma\tau^x, \tag{2.4a}$$
$$\varepsilon\left[\frac{\partial V}{\partial t} + \nabla\cdot(V\mathbf{u})\right] =$$
$$-\varepsilon Fh\frac{\partial h}{\partial y} - (1+\varepsilon\beta y)U + E\nabla^2 V - \mu V, \tag{2.4b}$$
$$\frac{\partial h}{\partial t} + \frac{\partial U}{\partial x} + \frac{\partial V}{\partial y} = 0, \tag{2.4c}$$

where all the variables are nondimensional and the primes have been dropped. The nondimensional parameters are: the Rossby number $\varepsilon = U^*/(f_o L)$, the Froude number $F = g'H/(U^*)^2$, the Ekman number $E = A/(f_o L^2)$, the nondimensional Rayleigh viscosity coefficient $\mu = R/f_o$, $\beta = \beta_o L^2/U^*$, the nondimensional wind-stress amplitude $\sigma = \tau_o/(f_o H U^* \rho)$, and the basin aspect ratio $\nu = D/L$.

By moving the nonlinear term to the right-hand side of Eqs. (2.4)

$$\frac{\partial U}{\partial t} = -\nabla\cdot(U\mathbf{u}) - Fh\frac{\partial h}{\partial x} + \left(\varepsilon^{-1} + \beta y\right)V$$
$$+ \varepsilon^{-1}E\nabla^2 U - \varepsilon^{-1}\mu U + \varepsilon^{-1}\sigma\tau^x, \tag{2.5a}$$
$$\frac{\partial V}{\partial t} = -\nabla\cdot(V\mathbf{u}) - Fh\frac{\partial h}{\partial y} - \left(\varepsilon^{-1} + \beta y\right)U$$
$$+ \varepsilon^{-1}E\nabla^2 V - \varepsilon^{-1}\mu V, \tag{2.5b}$$
$$\frac{\partial h}{\partial t} = -\frac{\partial U}{\partial x} - \frac{\partial V}{\partial y} \tag{2.5c}$$

and discretizing in space, it is possible now to write the system (2.5) in a general, compact vector form

$$\frac{d\mathbf{W}}{dt} = \mathbf{F}(\mathbf{W};\mathbf{P}), \tag{2.6}$$

where $\mathbf{W} = (U,V,h)$ is the state-variable vector, $\mathbf{F} = (f_1, f_2, f_3)$ is the corresponding right-hand side vector, and $\mathbf{P} = (\beta, \varepsilon, \sigma, \mu, \nu, E, F)$ is the p-dimensional vector of parameters. The discretization here is by finite differences [see details in Jiang (1994)], so $\mathbf{W}$ is a d-dimensional vector consisting of the unknowns at the grid points and $\mathbf{F}$ is a nonlinear mapping $R^d \times R^p \rightarrow R^d$, where d indicates the number of discrete scalar variables in (2.6), considered as a system of ordinary differential equations (ODEs) for the components of $\mathbf{W}$.

The ODE system (2.6) is the object of this study. It is autonomous, i.e., the time variable does not occur in the right-hand side explicitly, since the forcing is constant in time. As a dynamical system, it is forced and dissipative (e.g., Lorenz, 1963; Ghil and Childress, 1987, Ch. 5). We shall investigate the system's attractors, their properties, and their relevance to the mid-latitude wind-driven oceanic circulation.

3 Numerical Methods

We study first the model's stationary solutions and follow their behavior as the parameters change. This will help us examine later the nonstationary flow regimes (Legras and Ghil, 1985; Ghil and Childress, 1987, Ch. 6).

A steady-state solution $\mathbf{W}$ of system (2.6) satisfies the set of nonlinear algebraic equations

$$\mathbf{F}(\mathbf{W};\mathbf{P}) = 0. \tag{3.1}$$

The number of equations here is very large, $d = O(10^4)$, and the numerical solution algorithm is comprised of two main parts: *(i)* the continuation method to advance one step along a branch of steady states as a parameter is varied, and *(ii)* an eigenvalue solver to determine the linear stability of the newly computed steady state.

3.1 Computation of Steady Flows in Phase-Parameter Space

To determine branches of steady solutions of (3.1) as one of the parameters (say λ) is varied, the pseudo-arclength continuation method (Keller 1977; Legras and Ghil 1985) is used. Knowing the solution of (3.1), $\mathbf{W}_o$, for a given parameter value λ_o, $\mathbf{F}(\mathbf{W}_o; \lambda_o) = 0$, one searches for solutions $\mathbf{W}(\lambda)$ near the point $(\mathbf{W}_o, \lambda_o)$ by using an approximate version of the implicit function theorem:

$$\frac{\partial \mathbf{F}}{\partial \mathbf{W}}\left(\mathbf{W} - \mathbf{W}_o\right) + \frac{\partial \mathbf{F}}{\partial \lambda}\left(\lambda - \lambda_o\right) = 0, \tag{3.2}$$

where $\partial\mathbf{F}/\partial\mathbf{W}$ and $\partial\mathbf{F}/\partial\lambda$ are matrices of partial derivatives evaluated at $(\mathbf{W}, \lambda) = (\mathbf{W}_o, \lambda_o)$. The particular

continuation method used here solves (3.2) as an ODE in the "arclength" s given by $ds^2 = \|d\mathbf{W}\|^2 + |d\lambda|^2$, using a predictor-corrector method: A given solution branch $(\mathbf{W}(s), \lambda(s))$ through $(\mathbf{W}_0, \lambda_0)$ is parametrized by the arclength s, to permit continuation around the turning points associated with saddle-node bifurcations. Here $\|\mathbf{W}\|$ stands for the length of the vector $\mathbf{W}$, in the appropriate dimension of Euclidean space, namely $d = 15000$.

The "evolution" equation along the branch is obtained by following the tangent

$$\dot{\mathbf{W}}_0^T(\mathbf{W} - \mathbf{W}_0) + \dot{\lambda}_0(\lambda - \lambda_0) - \Delta s = 0 \ ; \tag{3.3}$$

$(\mathbf{W}_0, \lambda_0)$ is a starting solution, known analytically or numerically, or a previously computed point on the given branch, Δs is the step length, and the dot stands for differentiation with respect to arclength s. To solve the system of equations (3.1, 3.3), Euler-Newton steps are taken (see the Appendix for details).

To monitor singularities on a particular branch, several indicator functions are used. Turning points are detected by following the slope of the tangent vector $(\dot{\mathbf{W}}, \dot{\lambda})$ along the branch. Other singularities, like Hopf bifurcation points, must be detected by solving the linear stability problem. For simple bifurcation points (i.e., transcritical or pitchfork bifurcations) there are computationally easier alternatives, for example it suffices to compute the sign of $\det(\partial\mathbf{F}/\partial\mathbf{W})$, instead of solving the linear stability problem at each point $(\mathbf{W}, \lambda)$ and computing all the eigenvalues (see Appendix).

3.2 Computation of the Linear Stability of a Particular Steady State

The discrete linear equations governing the evolution of infinitesimal disturbances on a particular steady state of the discretized nonlinear problem (3.1) lead to a generalized eigenvalue problem

$$\mathcal{A}\mathbf{x} = \eta\mathcal{B}\mathbf{x}, \tag{3.4}$$

where $\mathcal{A}$ and $\mathcal{B}$ are $d \times d$ matrices; in current fluid-dynamical applications $d = O(10^4$–$10^5)$, depending on the accuracy desired. A is, in general, nonsingular, while B is diagonal and may become singular, through the incompressibility condition.

Traditional eigenvalue solvers, such as the QZ algorithm, (e.g., Golub and Van Loan, 1989) – that determine all eigenvalues and, if desired, all eigenvectors – are impossible to use for problems of this size. In many hydrodynamic stability problems, the initial instability of a certain steady flow pattern occurs only through a few modes. In the discretized linear stability problem (3.4) one wishes, therefore, to compute a small number of eigenmodes, i.e., those with eigenvalues closest to the imaginary axis: the "most dangerous" modes. This motivated several studies to develop specific algorithms for the given task.

Table 1. Standard values for the dimensionless parameters in Eq. (2.6).

Parameter	Value
ε	$0.2 \cdot 10^{-1}$
σ	$0.2448 \cdot 10^{-2}$
E	$0.6 \cdot 10^{-5}$
μ	$1.0 \cdot 10^{-3}$
β	$2.0 \cdot 10^{1}$
ν	2
F	$1.55 \cdot 10^{1}$

Following Christodoulou and Scriven (1988), Dijkstra (1992) used a combination of the spectral transform and the Simultaneous Iteration Technique (Steward and Jennings, 1981), abbreviated here as SIT, do to so. The idea of the algorithm is to transform the eigenvalue problem in such a way that the most dangerous modes become dominant (i.e., have largest absolute value). In this way, generalized power methods (Golub and Van Loan, 1989) can be used on the transformed problem.

The first step of the eigenvalue algorithm is the application of a complex mapping to the generalized eigenvalue η,

$$\eta = b + a\frac{\kappa - 1}{\kappa + 1}, \tag{3.5}$$

where b is real and a is positive. The parameter b shifts the generalized spectrum along the real axis, whereas the parameter a stretches it. The left complex plane $\mathrm{Re}(\eta - b) < 0$ is mapped into the unit disk $|\kappa| < 1$, with the imaginary axis $\mathrm{Re}(\eta - b) = 0$ being mapped onto the unit circle $|\kappa| = 1$.

The eigenvalue problem (3.4) is transformed by (3.5) to

$$\mathcal{C}\mathbf{x} = \mathcal{D}\kappa\mathbf{x}, \tag{3.6}$$

where $\mathcal{C} = \mathcal{A} + (a - b)\mathcal{B}$ and $\mathcal{D} = -\mathcal{A} + (a + b)\mathcal{B}$ Although $\mathcal{B}$ is singular, the matrices $\mathcal{C}$ and are generically not singular and we therefore consider the problem

$$\mathcal{D}^{-1}\mathcal{C}\mathbf{x} = \kappa\mathbf{x}. \tag{3.7}$$

Equation (3.5) has the requisite property of mapping the most dangerous modes of (3.6) onto the dominant modes of (3.7); the eigenvalues $\eta = \infty$ are mapped onto $\kappa = -1$. SIT is particularly well suited to determine a prescribed number of dominant modes: It consists of a succession of filtering and reorientation stages. During a filtering stage, components in the direction of the dominant eigenmodes increase in amplitude. After each filtering stage, the reorientation stage finds an approximation to the eigenvalues λ and associated eigenvectors by solving an eigenvalue problem of small order with standard methods,

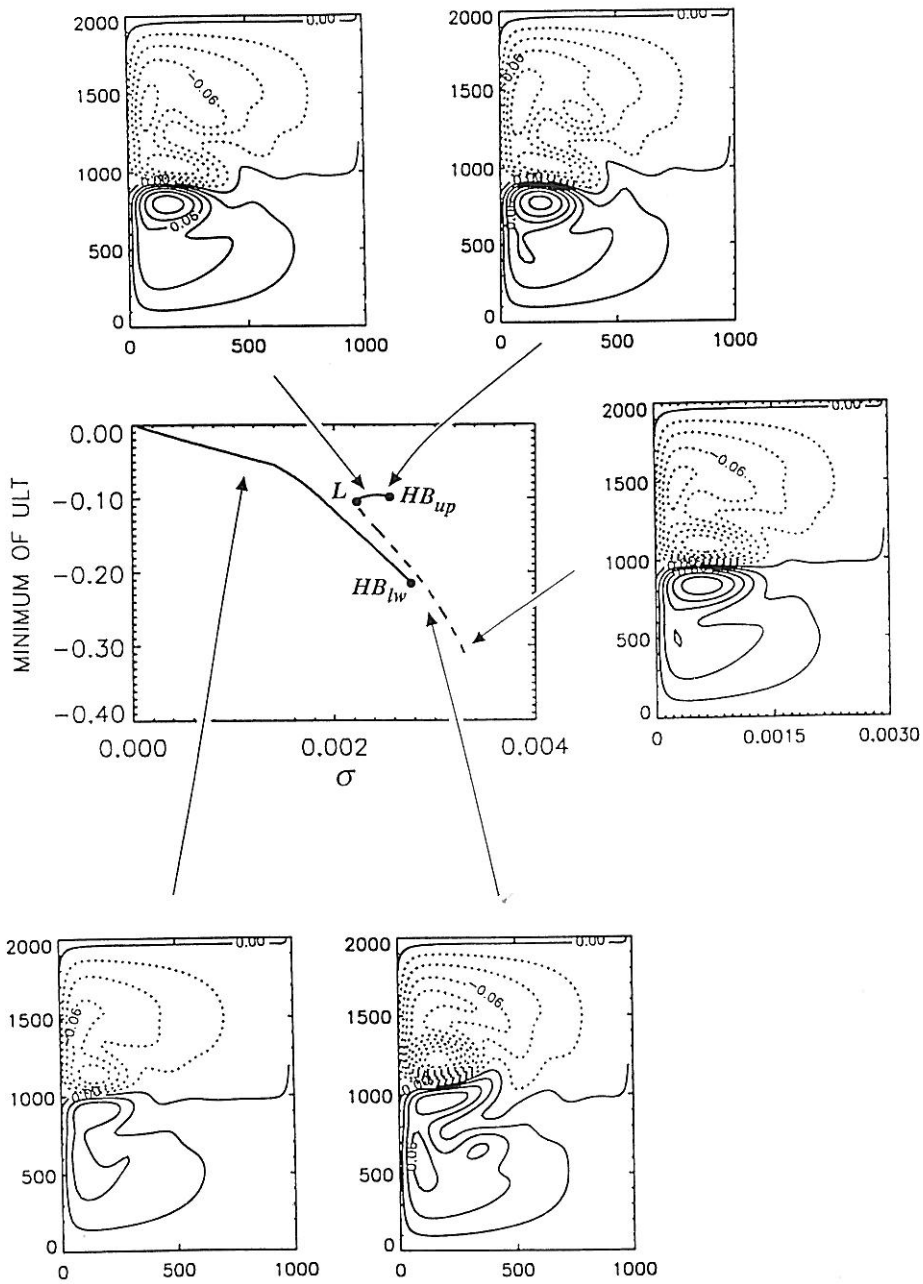

Fig. 1. Bifurcation diagram and flow patterns of steady solutions as a function of the forcing parameter σ . Other parameter values as in Table 1. Solid lines indicate stable, dashed lines unstable branches. Arrows point to the branch segment along which the solutions exhibit the flow pattern illustrated.

for instance QR (Golub and Van Loan, 1989). The combined filtering and reorientation process is performed a number of times, until convergence occurs according to a certain stopping criterion (Stewart and Jennings, 1981). The corresponding small number of accurate eigenvalues η of (3.4) are found from (3.5). Details are provided in the Appendix.

4 Stationary Solutions

The results are presented in the form of bifurcation diagrams, with the parameter under consideration on the abscissa and a quantity W characterizing the solution on the ordinate. JJG used for W the meridional position of the confluence between the two separated WBCs in their approximate bifurcation diagram. Since the exact position of this confluence point is hard to determine with precision, we use here for W the value of the minimum upper-layer thickness (ULT on the plots), i.e., the value of the shallow-layer thickness at the center of the strong cyclonic recirculating cell within the subpolar gyre, close to the confluence point. Solid lines indicate stable and dashed lines unstable branches. The singularities are labeled L for *limit* or turning points, i.e., saddle-node bifurcations, and HB for *Hopf bifurcation* points, respectively. Sometimes

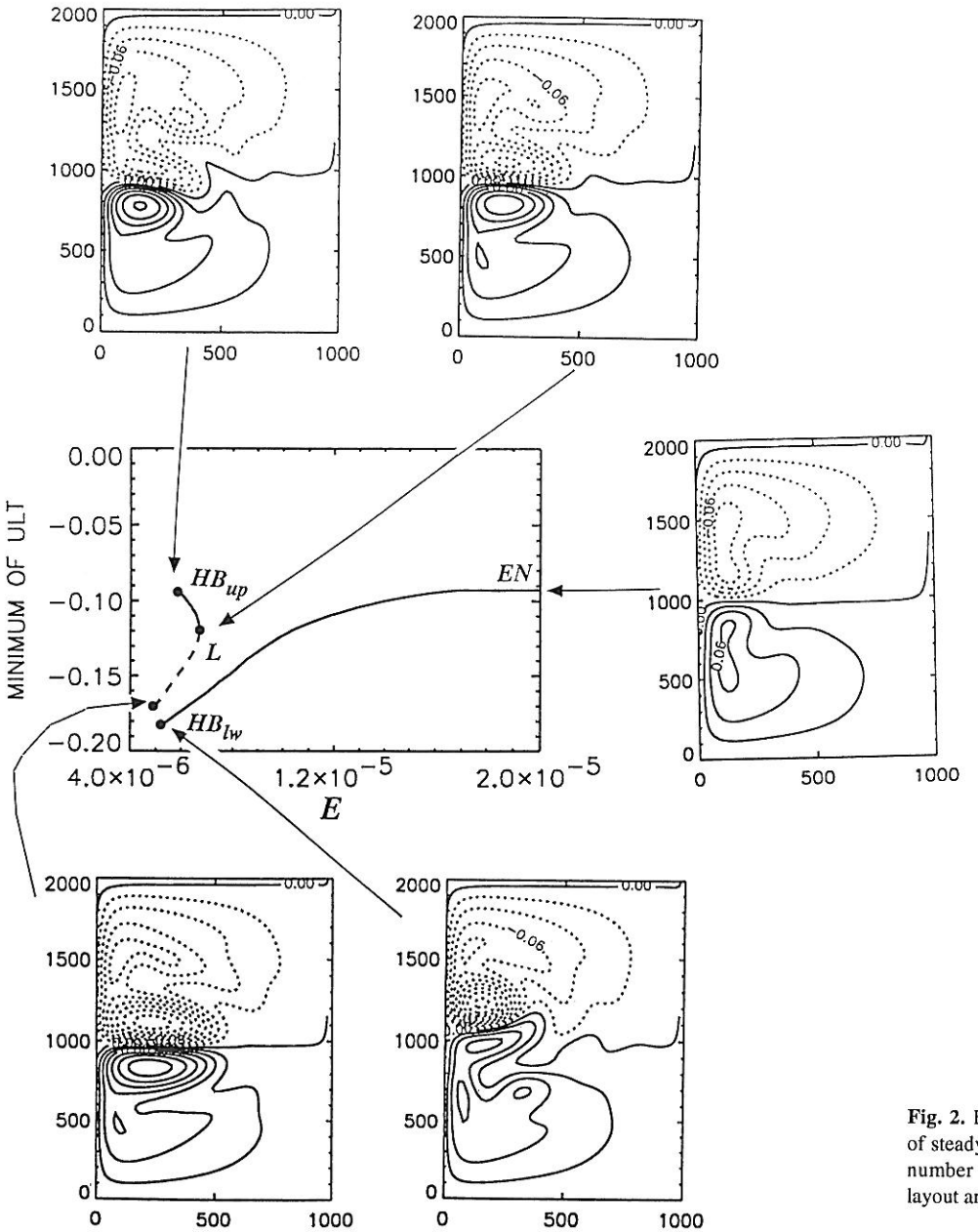

Fig. 2. Bifurcation diagram and flow patterns of steady solutions as a function of the Ekman number E. Other parameters as in Table 1; layout and labeling as in Fig. 1.

EN is used to denote a computational endpoint of a particular branch in the plot.

The patterns shown in the figures are contour plots of the deviation of the upper-layer thickness from its value at rest, i.e., from unity in nondimensional units. Solid lines are for positive and dashed lines for negative values. Following JJG, we call the basin's zonal axis of symmetry, along which the curl of the wind stress is zero, the *R*-line.

4.1 Bifurcation Structure for Increasing Wind Stress

The bifurcation diagram of steady solutions, as the wind-stress amplitude σ varies, is shown in Fig. 1. The values of the dimensionless parameters are listed in Table 1. Starting from the solution at rest, for which no forcing is present, we follow the branch for increasing values of σ. The branch of steady solutions that issues from the origin stays unique as long as the wind-stress amplitude is small. Along this branch, the minimum value of the upper-layer thickness decreases at first in a linear fashion. The flow pattern is nearly antisymmetric and related to the antisymmetric solutions that have been found in classical studies of the double-gyre wind-forced ocean (e.g., Veronis, 1966a; 1966b; Verron and Le Provost, 1991). The slight departure from exact antisymmetry is due to the tilting of the thermocline associated with a zonal flow (the eastward jet) on a β-plane, as documented already by the linear component of JJG's double-gyre model.

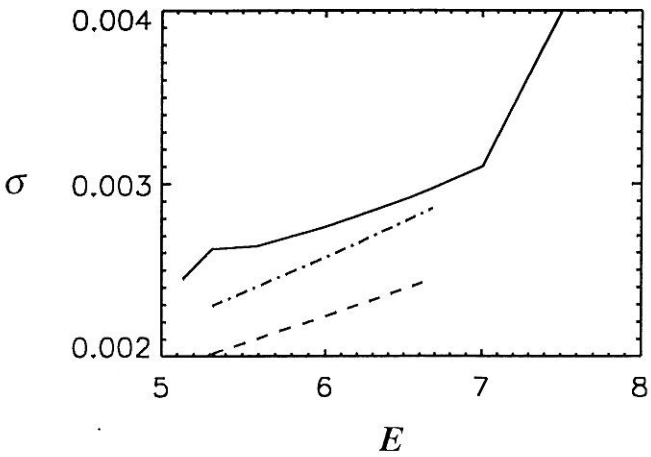

Fig. 3. Loci of the Hopf bifurcation points HB_{lw} (solid) and HB_{up} (dash-dotted) and the limit point L (dashed: see Fig. 1 for identification) as a function of the Ekman number E ; abscissa is $E{\cdot}10^6$.

As σ increases, the two recirculating cells – situated first against the western boundaries – become stronger and move slightly eastward. At $\sigma = 0.1410{\cdot}10^{-2}$, the branch undergoes an abrupt change of slope, as the rate of growth of the cyclonic cell's intensity increases. The circulation becomes more asymmetric, with the cyclonic cell markedly stronger than the anticyclonic one. The subtropical gyre's waters cross the R-line and wrap partially around the cyclonic cell's eastern part, pulled by its greater intensity.

Up to the value $\sigma = \sigma_L \equiv 0.2232{\cdot}10^{-2}$ the solution is unique, but multiple equilibria occur for $\sigma > \sigma_L$, since two additional solution branches exist in this range. One of these branches is stable (the upper branch), while the other (the intermediate branch) is unstable. This structure seems to arise as a perturbed pitchfork bifurcation (e.g., Guckenheimer and Holmes 1983). The latter is expected to occur in a system of equations having a reflection symmetry along the R-line [compare Quon and Ghil (1992) for multiple equilibria of an idealized, two-dimensional ocean's thermohaline circulation]. This bifurcation is not structurally stable and can be destroyed by small perturbations, as it happens in the present case, due to the slope of the sea surface and thermocline associated with the eastward jet on an β-plane. Indeed, the classical barotropic vorticity equations with double-gyre wind-stress forcing, as well as the associated boundary conditions, are symmetric with respect to the zero wind-stress curl axis, given here by $y = 0.5$; more precisely, the symmetry of the solutions about this axis is given by $U \rightarrow U$, $V \rightarrow -V$, and $h \rightarrow -h$). In this case, there is a pitchfork bifurcation on the symmetric branch that causes its loss of stability and the appearance of two new, stable solution branches (see Section 4b of JJG). The solutions along either branch are asymmetric and exhibit the same mirror symmetry *with respect to those on the other branch* as the solutions along the now unstable branch had with respect to themselves. On the contrary, in the present PE double-gyre formulation the basin-wide tilting of the thermocline is not invariant under reflection in the R-line [see also Section 3c and Appendix B of JJG].

The solutions on the upper branch are characterized by the anticyclonic cell being stronger and capturing through nonlinear advection a tongue of the subpolar water along its eastern edge across the R-line. In between the two stable branches – upper and lower – the nearly antisymmetric solutions reappear but they have lost their stability. This unstable branch merges with the upper branch at $\sigma = \sigma_L$. The upper and lower branch here are reversed with respect to the approximate bifurcation diagram of JJG (Fig. 3 there), as the confluence point lies above the R-line when the cyclonic recirculation cell is stronger, and hence its central thickness is smaller.

For three different values of the wind stress, each of the three steady-state branches passes through a Hopf bifurcation. The first to be destabilized are the solutions on the upper branch ($\sigma_{Hup} = 0.2572{\cdot}10^{-2}$), then the lower branch ($\sigma_{Hlw} = 0.2749{\cdot}10^{-2}$) and, finally, the unstable branch ($\sigma_{Hus} = 0.3330{\cdot}10^{-2}$).

4.2 Dependence on the Ekman Number

The impact of a varying viscosity coefficient on the multiplicity and stability of the solutions discussed in the previous subsection is considered next. The bifurcation diagram illustrating how the solutions vary with the viscosity parameter E for a fixed value of $\sigma = 0.24483{\cdot}10^{-2}$, with ε, μ , β, ν, and F as in Table 1, is plotted in Fig. 2. Once again, the structure of the diagram shows a perturbed pitchfork bifurcation. For large values of E, only the lower solution branch exists: the flow pattern is nearly

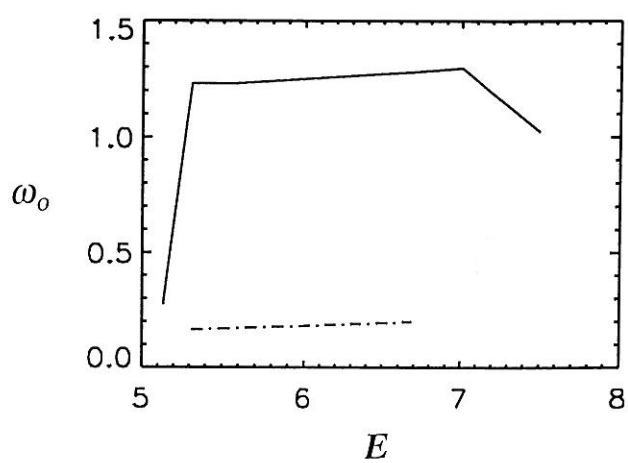

Fig. 4. Angular frequency ω_o of the oscillatory instability (radians per nondimensional time unit) along the Hopf bifurcation loci HB_{lw} (solid) and HB_{up} (dash-dotted) in Fig. 3.

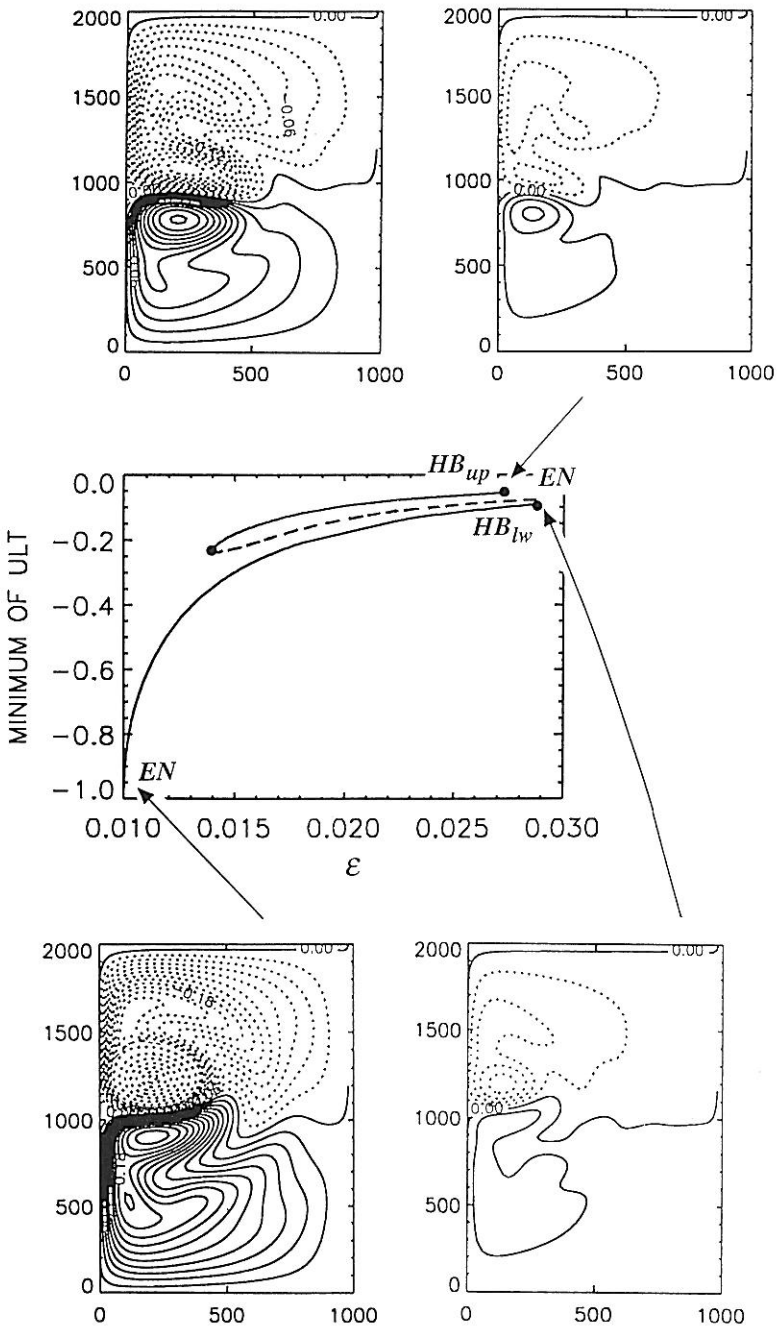

Fig. 5. Bifurcation diagram and flow patterns of steady solutions as a function of the Rossby number ε . Other parameters as in Table 1; layout and labeling as in Fig. 1.

antisymmetric and there is no strong recirculation. As the viscosity is decreased, the smaller-scale structures gradually reappear, being less dissipated. At $E_L = 6.69 \cdot 10^{-6}$, a turning point leads to a second fold. For $E < E_L$ three branches of solutions coexist. They present the same qualitative behavior as the three branches in Fig. 1. As in that diagram, each equilibrium branch leads to a Hopf bifurcation, at distinct values of E.

The loci of the turning point and Hopf bifurcation points in the (σ, E)-plane are shown in Fig. 3. The qualitative structure remains the same for each value of E . As the dissipation decreases, the Hopf bifurcations by which the lower branch (solid) and upper branch (dash-dotted) lose their stability approach slowly the turning point (dashed), i.e., the solutions on these branches can be destabilized more easily as the system becomes less dissipative, in accordance with our general fluid-dynamical intuition. For values of E larger than $7.0 \cdot 10^{-6}$, the slope of the HB_{lw} locus increases abruptly. The situation in which the northward WBC overshoots the R-line, i.e., the lower branch of the bifurcation diagram depicted in Figs. 1 and 2, seems therewith to be always stabler than the other solutions with which it coexists at the same parameter values. This higher stability of the model's subtropical gyre being dominant is in pleasant, but possibly coincidental, agreement with the observed relative size of the two gyres in every ocean basin.

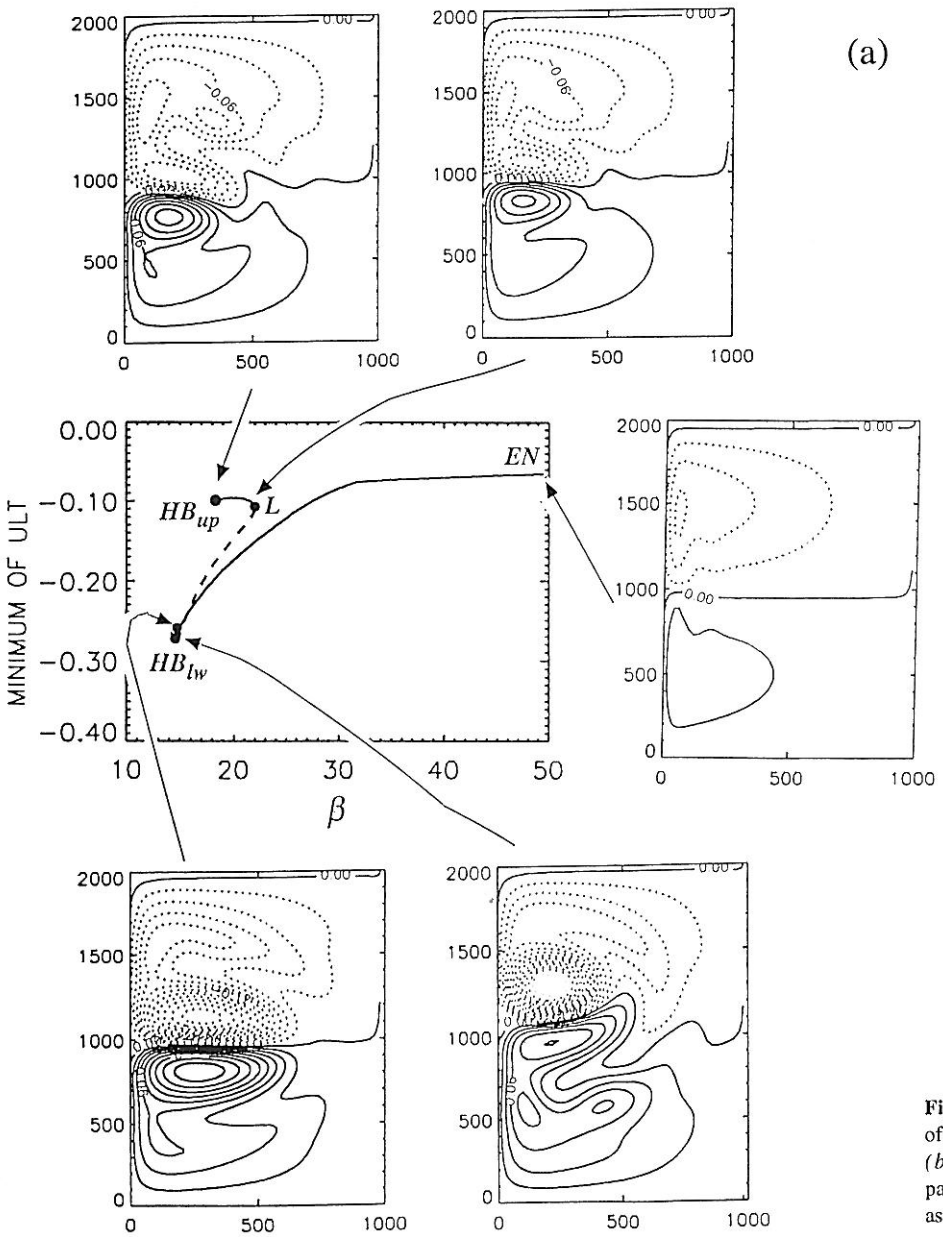

Fig. 6. Bifurcation diagrams and flow patterns of steady solutions as a function of: *(a)* β, and *(b)* the viscosity coefficient μ. Other parameters as in Table 1; layout and labeling as in Fig. 1.

The dependence of the angular frequency at Hopf bifurcation on E, along the bifurcation loci in Fig. 3, is shown in Fig. 4. For small values of E, the frequencies characterizing the oscillating behavior along the upper and lower branches are of the same order of magnitude. While the period of the Hopf bifurcation on the upper branch (dash-dotted) decreases but little with E, a rapid transition to higher frequencies characterizes the lower branch (solid) for values of E between $5.0 \cdot 10^{-6}$ and $5.5 \cdot 10^{-6}$. After this transition, the periods characterizing the two Hopf bifurcations differ by an order of magnitude: order of a few weeks for the lower branch and about 30 months for the upper one. The frequencies along the two branches increase linearly and very slowly with E until $E = 7.0 \cdot 10^{-6}$. Thereafter, the oscillation frequency for the lower branch decreases again, while we did not compute the upper-branch frequency behavior for larger values of E.

4.3 Dependence on the Rossby Number, on Beta, and on the Bottom Friction

The behavior of the solutions as the Rossby number ε varies is presented in Fig. 5 for all other parameter values as in Table 1. For small values of ε, only the lower branch of solutions exists. As the nonlinearities increase, the unstable branch (dashed) and the upper stable branch develop. For this parameter, too, the solutions transfer their stability from steady to periodic behavior. Hopf

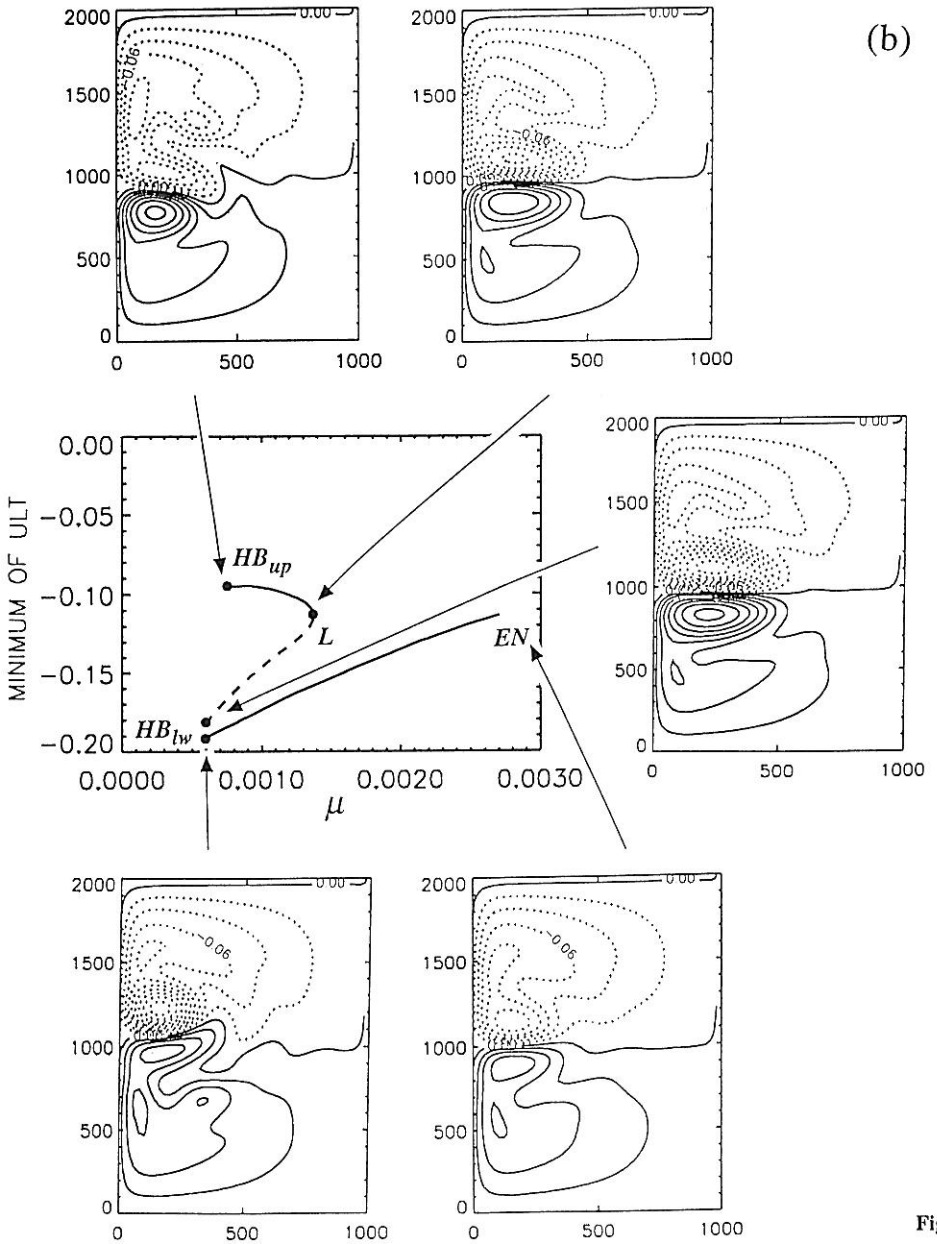

Fig. 6(b). For caption see preceding page.

bifurcations arise for $\varepsilon = 0.2653 \cdot 10^{-1}$ on the upper branch and $\varepsilon = 0.2846 \cdot 10^{-1}$ on the lower one.

The bifurcation structure of the solutions is presented for a varying β in Fig. 6a and for a varying bottom friction μ in Fig. 6b; all other parameter values are as in Table 1. For both of these parameters, as it was the case for a varying Rossby number, Ekman number, and wind forcing, a perturbed pitchfork bifurcation as well as the transition from stable or unstable steady states to periodic solutions through Hopf bifurcations characterize the behavior of the system. For large values of μ and β, only the stable steady solution with dominant subtropical gyre obtains. For smaller values of these two parameters – more precisely, for $\beta < \beta_L = 21.9420$ and for $\mu < \mu_L = 0.1373 \cdot 10^{-2}$ – the unstable and upper stable branch arise. The Hopf bifurcations are located, in Figs. 6a and 6b respectively, at $\beta_{HBup} = 18.6410$ and $\mu_{HBup} = 0.7948 \cdot 10^{-3}$ on the upper branch and at $\beta_{HBlw} = 14.4526$ and $\mu_{HBlw} = 0.6348 \cdot 10^{-3}$ on the lower branch.

The behavior of the solutions as μ varies does not differ, qualitatively, from that in Fig. 1, whereas some differences appear as β varies. Indeed, the flow pattern at the Hopf bifurcation point on the lower branch in Fig. 6b shows a striking increase in size of the major dipole structure, across the detached jet, and a greatly increased strength of the subpolar with respect to the subtropical recirculation. On the contrary, the structure of the circulation at the Hopf bifurcation point on the upper branch does not differ very

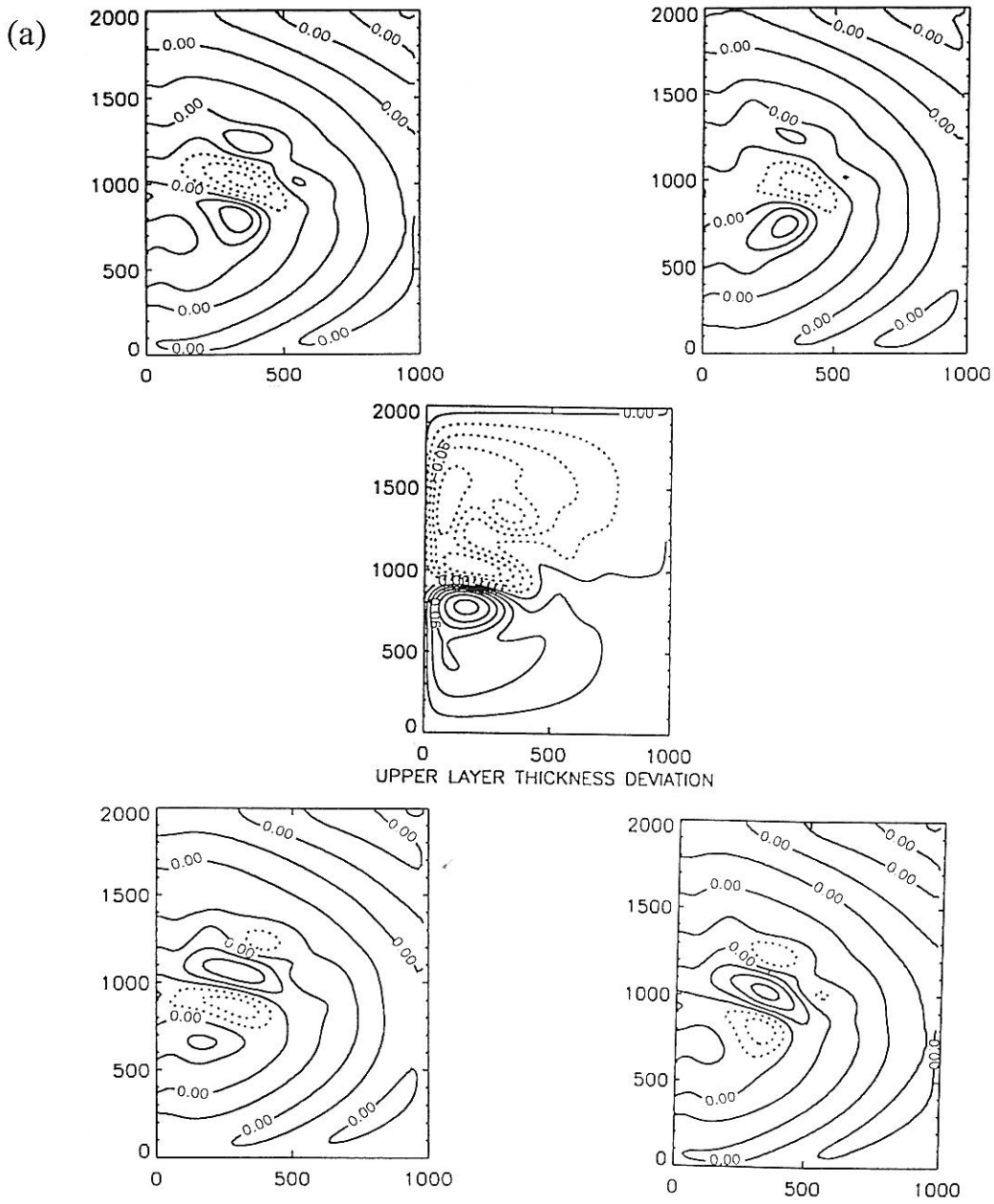

Fig. 7. Transition patterns at the Hopf bifurcations together with the basic state (center panel): *(a)* for HB_{up}; *(b)* for HB_{lw} (see Fig. 1 for location of HB_{up} and HB_{lw}). The time is in units of π/ω_o; $t = 0$ in the plot at the top left, $t = 0.25$ at the top right, $t = 0.75$ bottom left, and $t = 1$ at bottom right. Contour interval is 0.02 (in dimensionless units); geographic coordinates in km.

much from those presented in the previous bifurcation diagrams.

5 Hopf Bifurcation and Periodic Solutions

Time-periodic solutions branch off the Hopf bifurcation points. The spatial structure of these periodic solutions can be determined, close to their onset, by investigating the eigenvectors $(\mathbf{w}_1,\mathbf{w}_2)$ corresponding to the pair of complex conjugate eigenvalues which cross the imaginary axis at $(\pm i\omega_o)$. This time-periodic linear transition state is given by

$$\Psi(t) = \sin(\omega_o t)\mathbf{w}_1 - \cos(\omega_o t)\mathbf{w}_2, \quad 0 \le t \le 2\pi/\omega_o \quad (5.1)$$

In Fig. 7a, contours of the deviation of the upper-layer thickness are plotted in the four corner panels at four equidistant times t (in units of π/ω_o) for the transition state at the point H_{up}; $\sigma = \sigma_{Hup} \equiv 0.2572 \cdot 10^{-2}$ and all other parameter values are as in Table 1. The steady basic state upon which the oscillatory instability grows is shown in the center panel. In Fig. 7b, the transition structure is plotted for the Hopf bifurcation point on the lower branch H_{lw}, $\sigma = \sigma_{Hlw} \equiv 0.2749 \cdot 10^{-2}$. The evolution in time of the two transition structures is similar, except for the location in space of the main features.

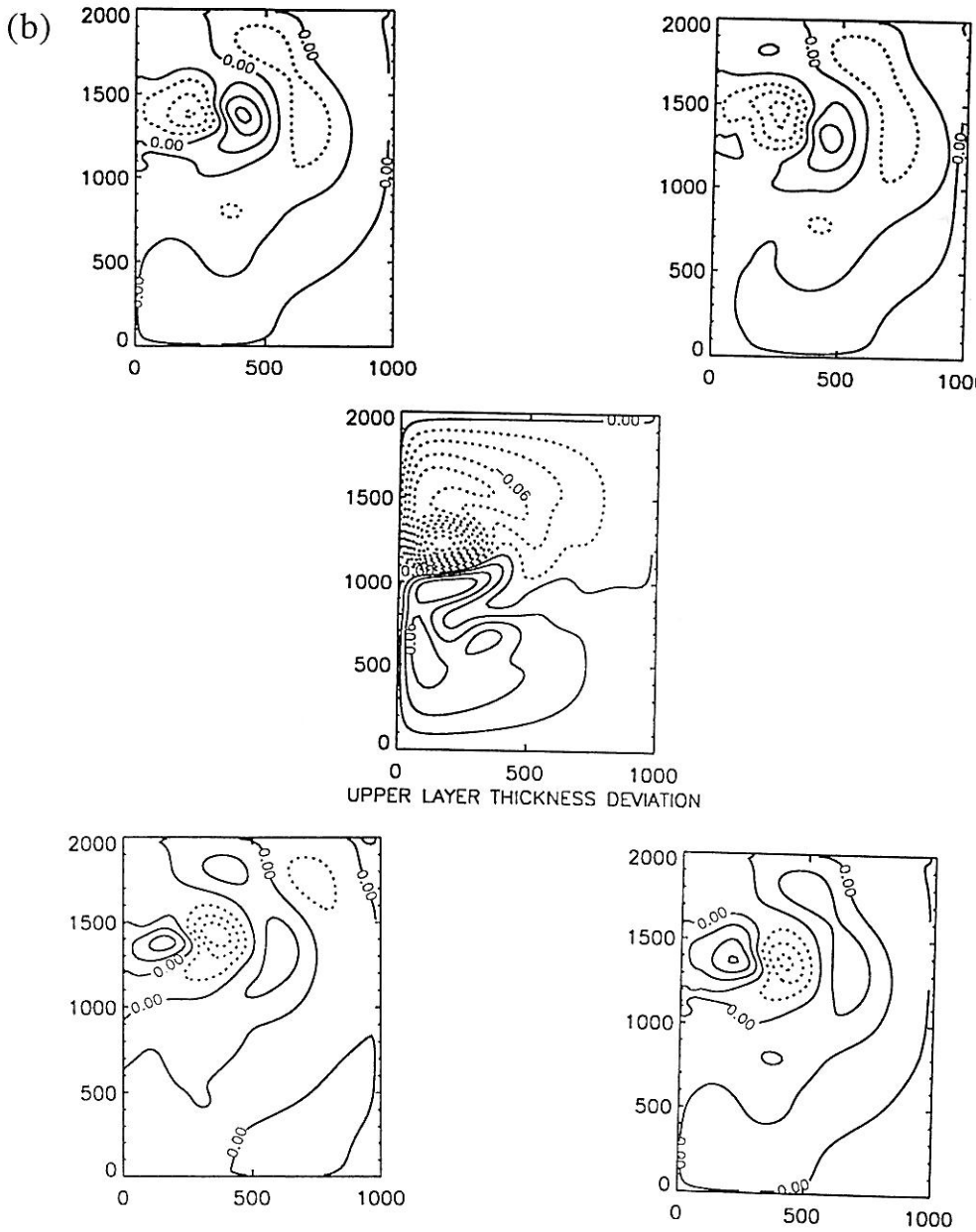

Fig. 7(*b*). For caption see preceding page.

The destabilizing mechanism appears to be related with Rossby-wave-like features and their finite-amplitude saturation as interacting multipole vortices. For both branches, the strongest features of the transition state are located over or close to the corresponding dominant recirculation cell. In panel (a) (upper branch) the approximate symmetry axis of the alternating-sign features is oriented roughly SW–NE, while in panel (b) (lower branch) it is more nearly W–E. The wave length of the fastest-growing perturbation is slightly shorter for the upper branch while the period is much longer, $\omega_o{}^{up} = 0.1804$ radians per nondimensional time unit vs. $\omega_o{}^{lw} = 1.248$ radians per nondimensional time unit for the lower. The differences are probably due to the different balances between internal, dispersive and forcing terms in the case where the cyclonic (lower branch) vs. the anticyclonic (upper branch) recirculation dominates. These balances favor different "wave guides" for the forced-dissipative, standing wave trains observed, and different nonuniform background flows in each wave guide. We also note that the spatial features of the variability decay rapidly away from the active separation, confluence and recirculation area; this observation justifies *a posteriori* the use of such a small basin size by JJG and through all but section 6.2 here.

A physical explanation of the destabilization process can be provided by analyzing the time-dependent behavior of the total field for a periodic solution, obtained asymptotically

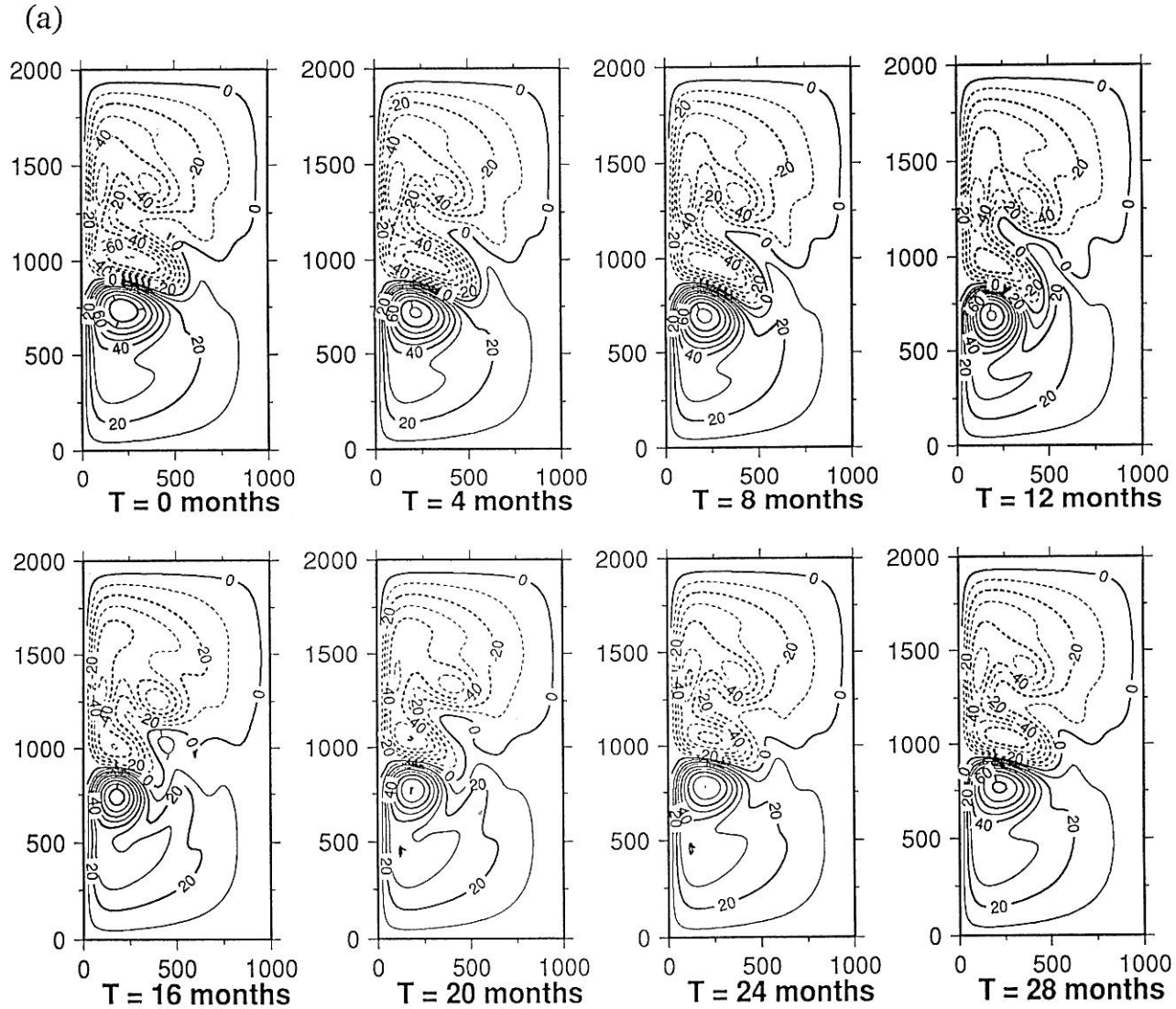

Fig. 8. Snapshots for a periodic solution obtained by forward integration of the model equations, for parameter values above the Hopf bifurcation on the upper branch ($\sigma = 0.3131 \cdot 10^{-2}$, other parameters as in Table 1). The interval between the snapshots is one- eighth of the cycle's period ($T = 32$ months in dimensional units). *(a)* Upper-layer thickness deviations (from the value of $H = 500$ m at rest); contour interval is 10 m. *(b)* Vorticity anomaly (from the values of the time-mean state); contour interval is 0.005 s^{-1}.

by forward integration. For the sake of brevity, we illustrate only a periodic solution belonging to the upper branch, on which the subpolar gyre is dominant in size with analogous arguments likely to apply to the lower branch. In Fig. 8a are plotted snapshots of the upper-layer thickness deviation for $\sigma = 0.3131 \cdot 10^{-2}$, at each eighth of a period T of the oscillatory cycle, $T = 34.8$ months in dimensional units.

For the solutions on the upper branch, the amplitude of the thickness deviations in the anticyclonic recirculation cell is larger than that in the cyclonic one. The two cells thus form an asymmetric dipole and interact nonlinearly across the zone where the two WBCs merge and form an intense eastward jet. Due to the asymmetry, the anticyclone drags the cyclone southeastward ($t = 0 - 4.35$ months) ; this aspect of asymmetric dipole behavior is well-known from laboratory studies (e.g., Flierl et al., 1983; Nguyen Duc and Sommeria, 1988; Fedorov et al., 1989; Van Heijst and Flor, 1989), as well as from theoretical and numerical studies (e.g., Flierl et al., 1980; Legras, 1992; Speich et al., 1995b). As the cyclone begins to penetrate further across the symmetric line, it drags in turn northwestward some "warm" water (characterized by the anticyclonic vorticity of the subtropical gyre in this adiabatic model) along it southeastern boundary, by analogous nonlinear interactions ($t = 8.70 - 13.05$ months).

As a consequence of this tripole interaction, the southward penetration of the cyclonic cell is slowed down,

(b)

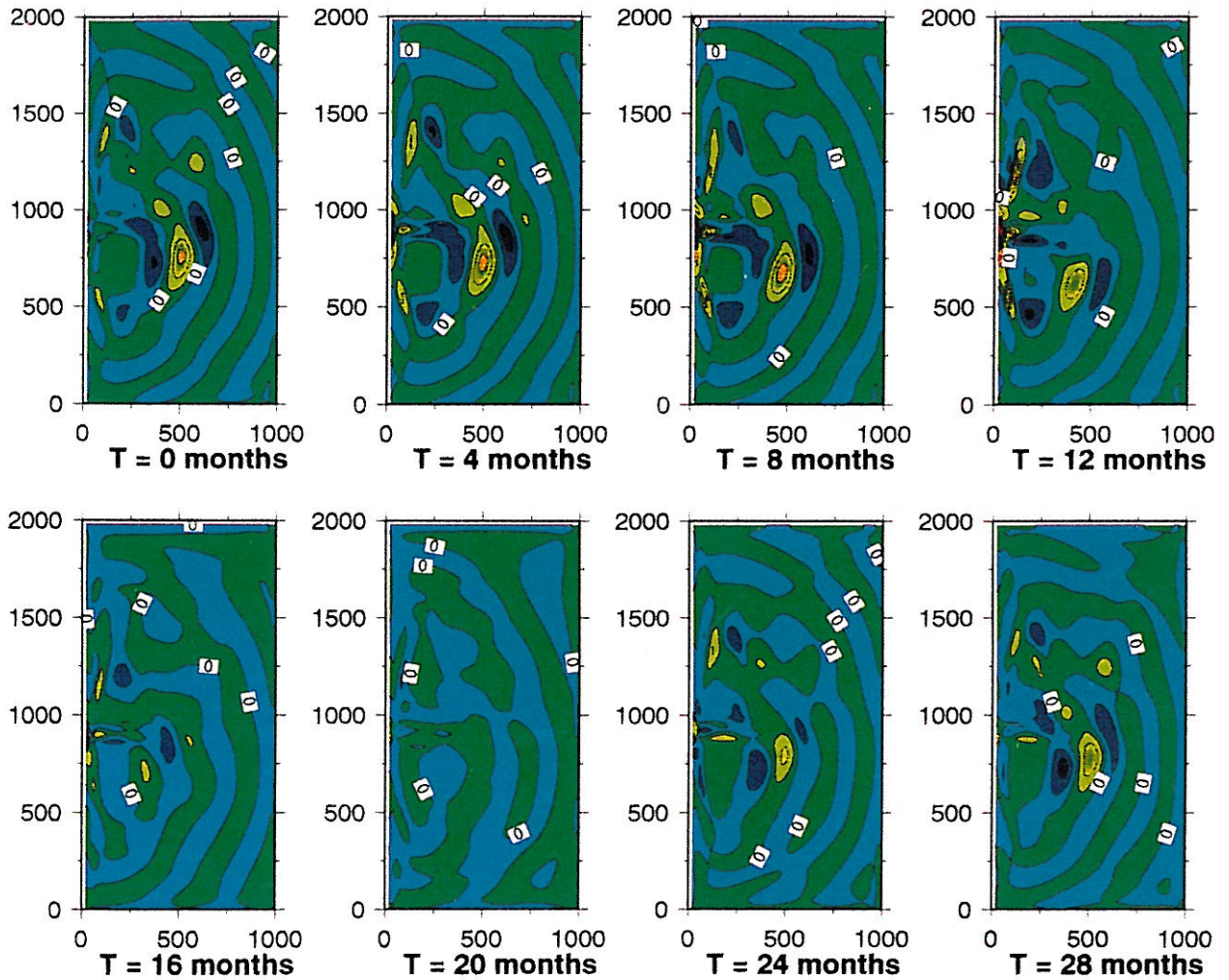

Fig. 8*(b)*. For caption see preceding page.

and the cyclone begins to retract to its initial position extending just south of the R-line ($t = 17.40 - 21.75$ months). In the meantime, the tongue of "warm" water penetrates deeper into the subpolar gyre, until it reaches a small recirculating cyclonic cell – manifest as a distortion of the contour lines in the north-central region – and a nonlinear interaction starts between the two cells of opposite vorticity.

A quadrupolar structure characterizes now the flow structure ($t = 26.10 - 30.45$ months) and acts to dissipate the positive vorticity associated with the "warm" water that has penetrated north of the R-line. The corresponding vorticity anomalies are plotted in Fig. 8b and document further the description just given. Consequently, the flow finds itself again in the unstable dipole configuration where a stronger anticyclonic cell interacts nonlinearly with a weaker cyclone through the eastward jet, pulling "cold" water southward, and the sequence of counterflow to the north, with formation and dissipation of additional vortices, starts over again.

In Fig. 9 are shown the anomalies of the upper-layer thickness that correspond to the total fields shown in Fig. 8a, i.e., the difference between the instantaneous fields and the limit cycle's mean state. The good agreement with the periodic evolution of the eigenvectors in Fig. 7a reinforces the hypothesis of Rossby-like wave growth, local steepening and multipole interactions as the physical mechanism responsible for the destabilization of the steady

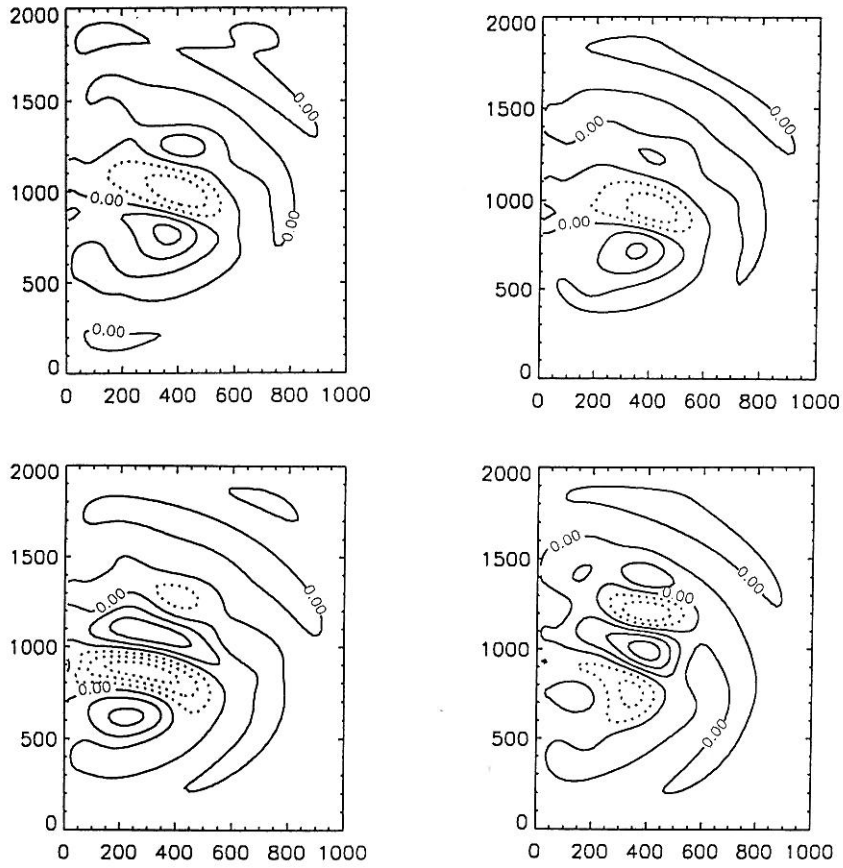

Fig. 9. Upper-layer thickness anomalies for the periodic solution obtained by direct integration with $\sigma = 0.3131 \cdot 10^{-2}$. The panels are ordered as in Fig. 7. Contour interval is 0.02 (in dimensionless units).

state and the saturation of the oscillatory instability. Both figures also show clear outward propagation of approximately concentric wave fronts from the most active part of the flow field to the outer, more quiescent reaches of the domain.

6 Transition to Aperiodic Solutions and Comparison with Observations

6.1 Limit Cycles and Chaotic Solutions

In section 5, we have seen how stationary solutions lose their stability by Hopf bifurcations which give rise to periodic solutions. In order to gain insight into the behavior of the flow for parameter values beyond the Hopf bifurcation points, a number of numerical integrations of the evolution equations (2.1) were carried out. This numerical study is not exhaustive but provides a reasonably good qualitative picture of model behavior in certain regions of phase-parameter space; these regions are either physically more realistic, since the real ocean belongs to this parameter space range, or else they are explored to complete our knowledge of possible model behavior types.

The stability transfer from stable stationary solutions to stable periodic solutions occurs through *supercritical* Hopf bifurçation for most of the parameters studied, with a stable equilibrium giving way to a stable limit cycle, whether for increasing σ values or decreasing E values (see Ghil and Tavantzis, 1983, p. 1040). To illustrate how the behavior of solutions changes across these Hopf bifurcations, evolution of the trajectory as σ increases is shown in Figs. 10 a–d. The phase-space trajectory is projected onto a plane spanned by the potential (x-axis) and kinetic (y-axis) energies. The solutions presented in the four panels belong to the upper branch of the bifurcation diagram in Fig. 1.

For values of σ smaller than at the Hopf bifurcation, the model trajectories converge to a fixed point (Fig. 10a); they converge to a simple, oval-shaped limit cycle for a narrow range of parameter values above the Hopf bifurcation (Fig. 10b). This limit cycle grows in size and its shape becomes more distorted for larger values of σ (Fig. 10c). As σ grows further (Fig. 10d), kinks develop in the limit cycle, and the trajectory no longer asymptotes to a closed orbit; in this latter case, the behavior of the solutions is deterministically aperiodic. Regularities are still present in such a solution, e.g., intermittent spells of quasi-stationary evolution or regular oscillations. This typically happens when weakly unstable fixed points or periodic orbits are contained within the (presumably strange) attractor, as shown for large-scale atmospheric flows by Legras and Ghil (1985), in an intermediate-resolution model, and by Kimoto and Ghil

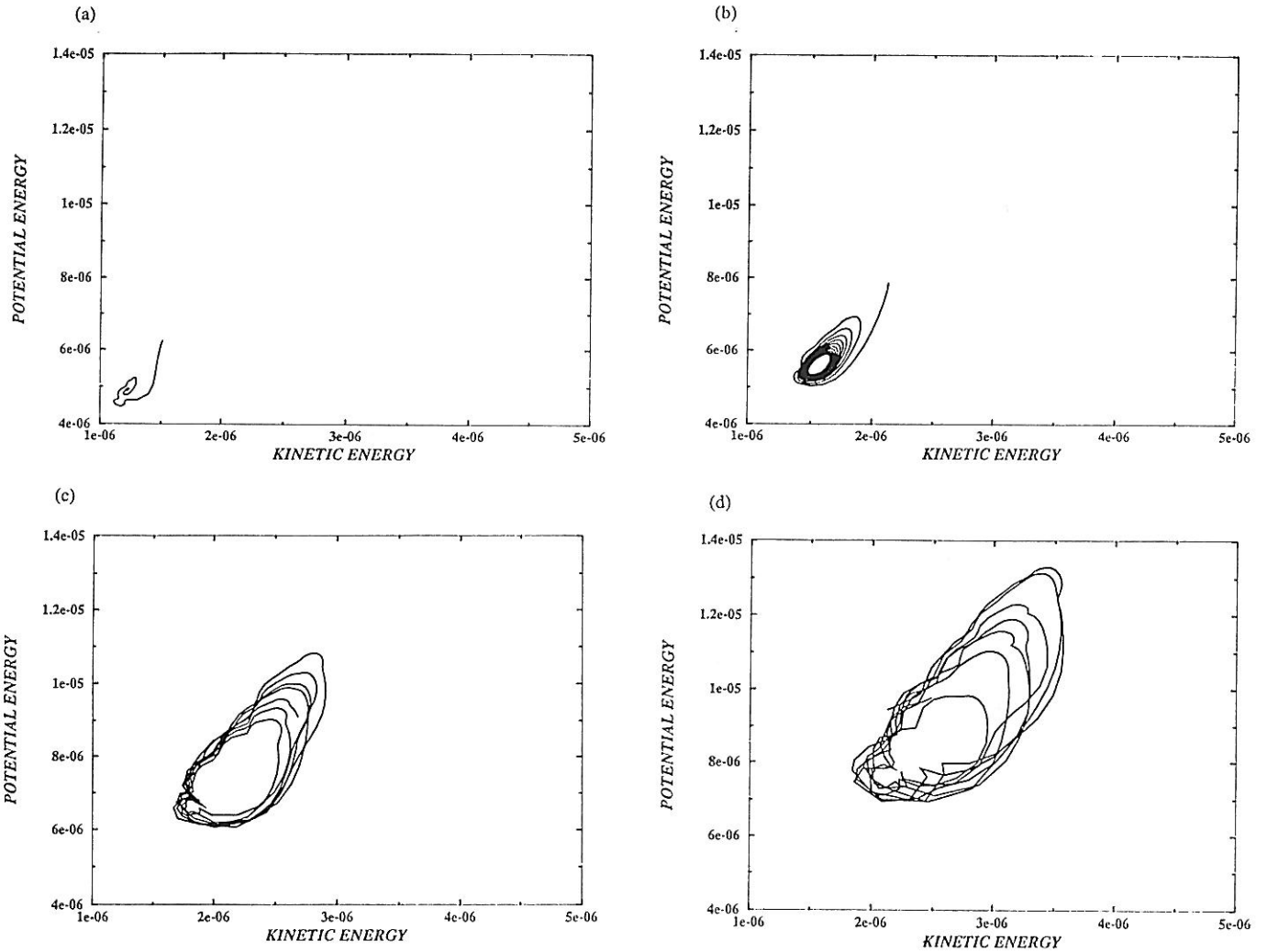

Fig. 10. Evolution of the trajectory projected on the phase plane defined by the potential (x-axis) and kinetic (y-axis) energies, as the wind stress σ increases: *(a)* $\sigma = 0.2544 \cdot 10^{-2}$; *(b)* $\sigma = 0.2818 \cdot 10^{-2}$; *(c)* $\sigma = 0.3131 \cdot 10^{-2}$; and *(d)* $\sigma = 0.3327 \cdot 10^{-2}$. Other parameters as in Table 1.

(1993a; 1993b) in a 40-year data set. The detailed exploration of the present system's irregular behavior is left for future work.

6.2 Dependence on Basin Size and Observational Validation

The most striking difference among ocean basins, the North Atlantic and North Pacific, say, is their difference in size. We carried out, therefore, sensitivity studies with respect to varying aspect ratio and total basin dimensions, through forward integrations of (2.1) using different parameter values.

First, we slightly increased the zonal dimension L of the basin, while keeping its meridional dimension D fixed. The behavior of the solutions for the resulting aspect ratio ν equal to 2.00, 1.82 and 1.67 is shown in terms of the potential- and kinetic-energy evolution in Figs. 11a and b, respectively. The solutions pass from purely periodic, nearly sinusoidal oscillations for $\nu = 2$ to a more and more aperiodic and anharmonic behavior for smaller values of this parameter. Furthermore, as the zonal extent of the domain increases and thus ν decreases, the dominant period, as well as amplitude, of the oscillations increases. This is rendered even more obvious by the kinetic energy's power spectra shown in Fig. 12: the broad spectral peak shifts from 32 months to 62 months and on to 77 months.

To compare the numerical results with the observed circulation of an ocean basin, we performed a numerical integration of system (2.1) for a rectangular basin close in size to the North Atlantic; its double-gyre circulation extends roughly from 20 N to 60 N. All parameter values are those of Table 1 except for $\sigma = 0.2074 \cdot 10^{-2}$, while $L = 6400$ km and $D = 4440$ km. The spatial resolution of the model is kept the same as in all the previous experiments, $\Delta x = \Delta y = 20$ km. The state variables evolve irregularly in this simulation, as shown in Figs. 13a,b for the potential (panel a) and kinetic (panel b) energy. Nevertheless, the system's trajectory is trapped in a

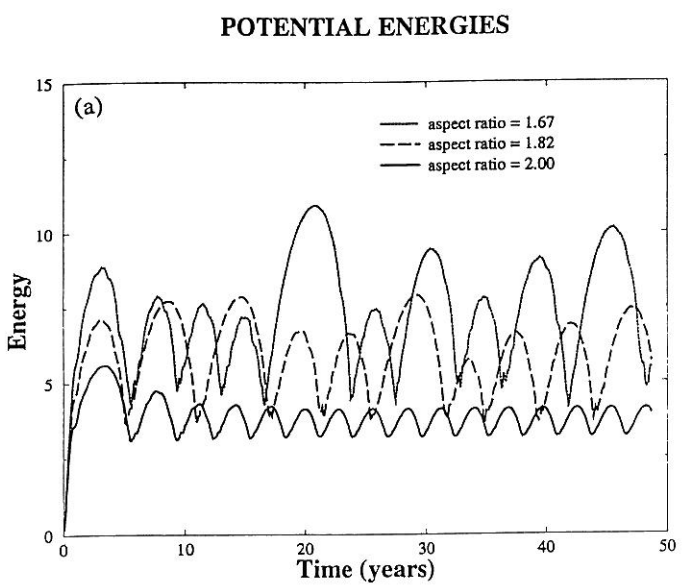

Fig. 11. Time evolution of (*a*) potential (PE) and (*b*) kinetic energy (KE) for varying aspect ratio ν : $\nu = 2$ (solid); $\nu = 1.82$ (dashed); and $\nu = 1.67$ (dotted). The diagrams are presented in dimensional units, with PE and KE in 10^{12} J m^{-2}.

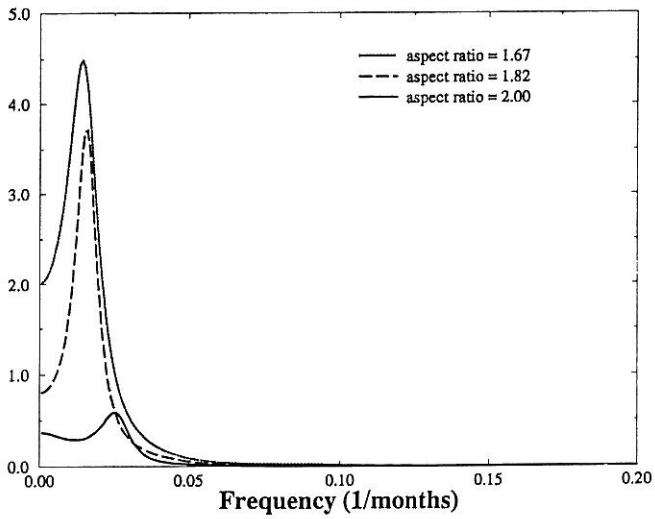

Fig. 12. Maximum-entropy spectra of the kinetic-energy time series of Fig. 11b. The order of the method (number of monthly lags) is 20. Solid line : $\nu = 2$; dashed line : $\nu = 1.82$; dotted line : $\nu = 1.67$. The peaks are located respectively at 32, 62, and 77 months, respectively.

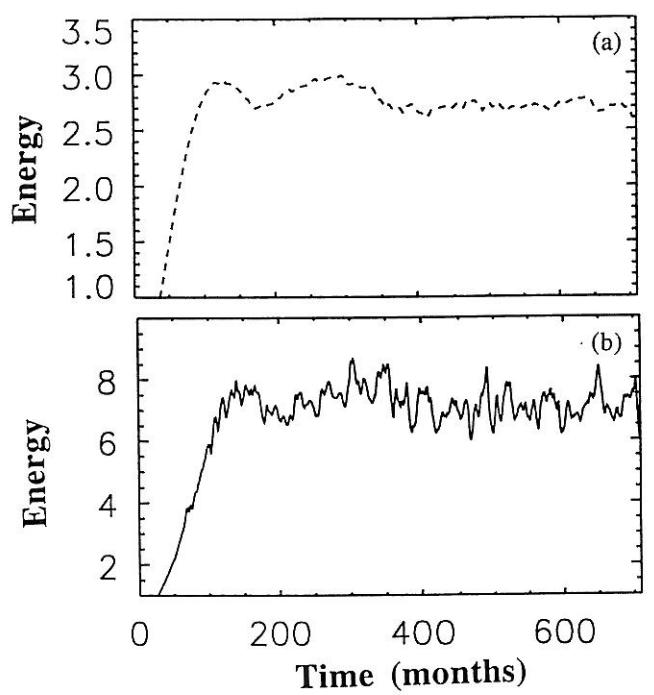

Fig. 13. Time evolution of *(a)* potential (PE) and *(b)* kinetic (KE) energy in a direct flow simulation for a basin size of $6400 \cdot 10^3$ m $\times$ $4400 \cdot 10^3$ m, $\sigma = 0.2074 \cdot 10^{-2}$; all other parameter values as in Table 1. The diagrams are presented in dimensional units, with PE in 10^{13} J m^{-2} and KE in 10^{11} J m^{-2}.

(1993a; 1993b) in a 40-year data set. The detailed exploration of the present system's irregular behavior is left for future work.

6.2 Dependence on Basin Size and Observational Validation

The most striking difference among ocean basins, the North Atlantic and North Pacific, say, is their difference in size. We carried out, therefore, sensitivity studies with respect to varying aspect ratio and total basin dimensions, through forward integrations of (2.1) using different parameter values.

First, we slightly increased the zonal dimension L of the basin, while keeping its meridional dimension D fixed. The behavior of the solutions for the resulting aspect ratio ν equal to 2.00, 1.82 and 1.67 is shown in terms of the

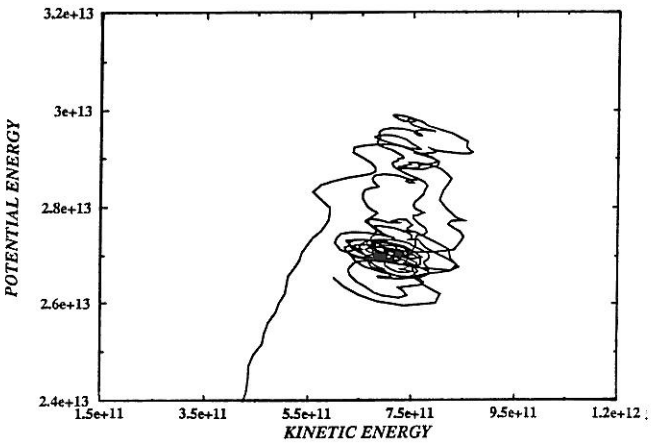

Fig. 14. Evolution of the system's trajectory projected as in Fig. 10. Same basin size and dimensional units as in Fig. 13.

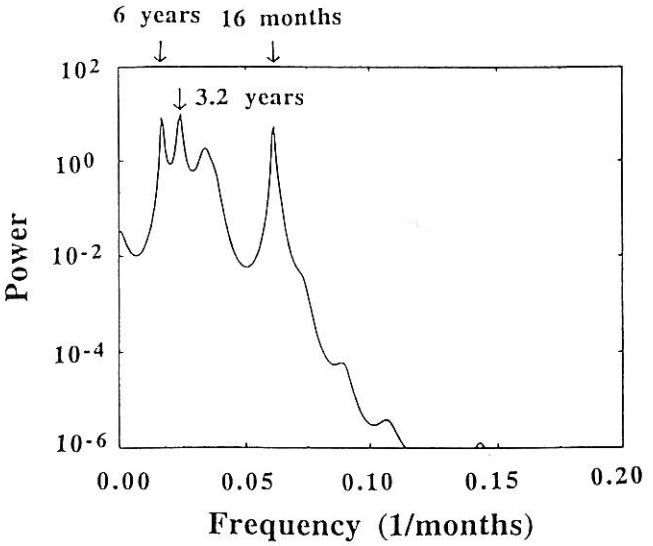

Fig. 15. Maximum-entropy spectrum of the kinetic-energy series in Fig. 13. Data-adaptive prefiltering was done by summing the eight leading reconstructed modes (see references in text for SSA details). The order of the method is 20.

potential- and kinetic-energy evolution in Figs. 11a and b, respectively. The solutions pass from purely periodic, nearly sinusoidal oscillations for $\nu = 2$ to a more and more aperiodic and anharmonic behavior for smaller values of this parameter. Furthermore, as the zonal extent of the domain increases and thus ν decreases, the dominant period, as well as amplitude, of the oscillations increases. This is rendered even more obvious by the kinetic energy's power spectra shown in Fig. 12: the broad spectral peak shifts from 32 months to 62 months and on to 77 months.

To compare the numerical results with the observed circulation of an ocean basin, we performed a numerical integration of system (2.1) for a rectangular basin close in size to the North Atlantic; its double-gyre circulation extends roughly from 20 N to 60 N. All parameter values are those of Table 1 except for $\sigma = 0.2074 \cdot 10^{-2}$, while $L = 6400$ km and $D = 4440$ km. The spatial resolution of the model is kept the same as in all the previous experiments, $\Delta x = \Delta y = 20$ km. The state variables evolve irregularly in this simulation, as shown in Figs. 13a,b for the potential (panel a) and kinetic (panel b) energy. Nevertheless, the system's trajectory is trapped in a relatively small region of phase space, as shown by the projection on the kinetic-potential energy plane in Fig. 14. To obtain additional information on the complicated behavior apparent from these figures, we subjected different global state variables to Singular Spectrum Analysis (SSA: Colebrook, 1978; Broomhead and King, 1986; Fraedrich, 1986; Vautard and Ghil, 1989). This analysis extracts a few principal modes of variability from the system's time series. SSA results for the kinetic-energy signal are presented in terms of the power spectrum of the time series, as reconstructed (Ghil and Vautard, 1991; Vautard et al., 1992) from its first eight modes (Fig. 15). The SSA window width chosen is of 120 months (i.e., 10 years).

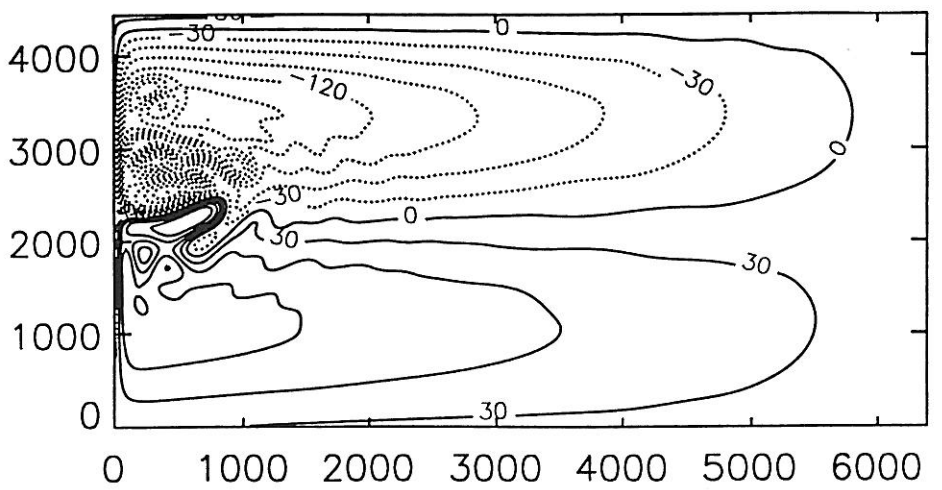

Fig. 16. Snapshot of the upper-layer thickness deviation after 35 years of integration for the experiment of Fig. 13. Contour interval is 30 m.

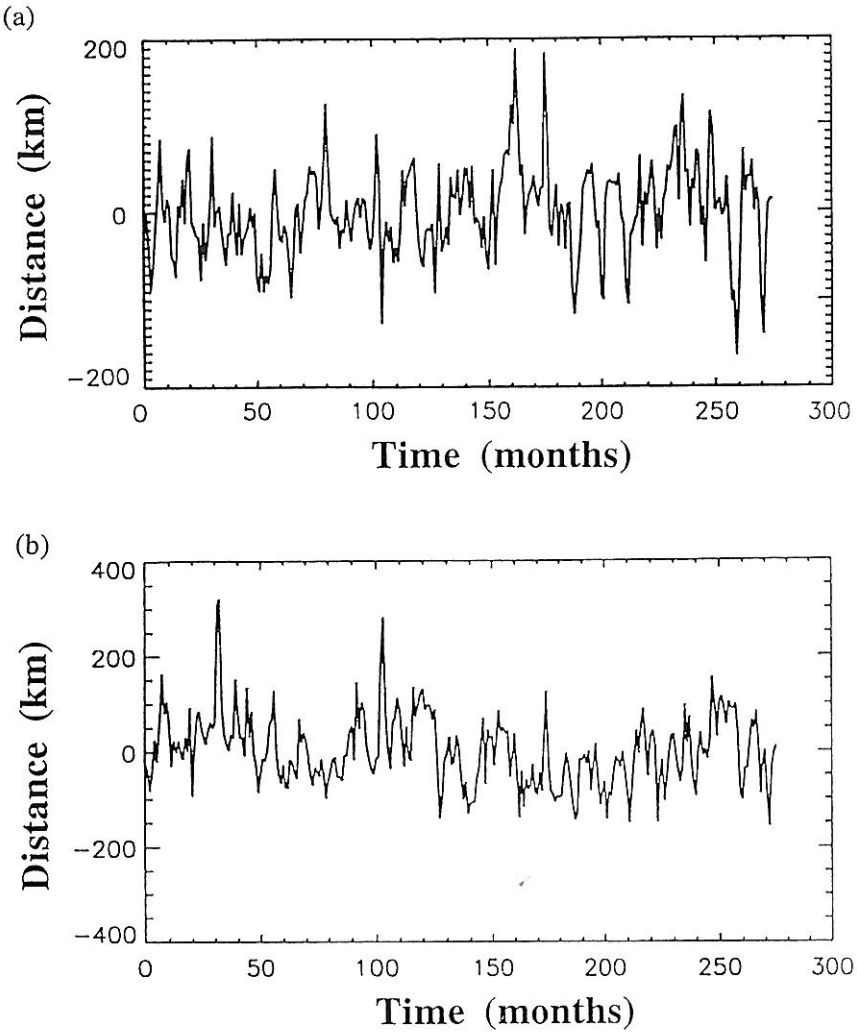

Fig. 17. Time evolution of the monthly meridional anomaly of the position of the sea-surface isotherm $T = 15$ °C from the latitude 40 N: *(a)* at 50 W (North Atlantic Ocean), and *(b)* at 146 E (North Pacific Ocean), from January 1970 to December 1992. The data are derived from the Comprehensive Ocean-Atmosphere Data Set (COADS). Meridional distance in km.

Three peaks clearly stand out; they correspond to the periods of 6 years, 3.2 years and 16 months, respectively.

The dynamics of the flow in this simulation is characterized by a high number of cyclonic and anticyclonic recirculation cells, as shown in a snapshot of upper-layer thickness deviation after 35 years of integration (Fig. 16). The multipole interactions, that lie at the root of the periodic and aperiodic solution behavior for the smaller basin previously discussed, reach here a higher degree of complexity, as the number of cells interacting with each other increases. This explains the much more irregular behavior of the solutions in the larger basin.

Still, the most vigorous flow features are concentrated near the separation of the WBCs and the confluence of the eastward jet, in a region not much larger than the 2000 km-by-1000 km basin we thoroughly analyzed. The intensity of the closed and open recirculation cells decays away from the separation and confluence points, in agreement with the concentrically decaying features in Figs. 7a and 9 here, as well as with the oceanic variability inferred from satellite altimetry (Fu et al., 1994; Speich and Ghil, 1994, and references there).

In order to get a first impression of how these numerical results compare with the real ocean, we have begun an exploration of the variability of the Gulf Stream and the Kuroshio Extension, close to their point of separation from the western boundaries. These areas are most active in both the real ocean [Fig. 3b of Speich and Ghil (1994)] and the present North Atlantic simulation (Figs. 13 – 16 here). In particular, we analyzed the position of these currents' axes. To do so, we calculated the monthly-mean distance of the meridional position of the sea-surface isotherm $T = 15°$ C from 40 N latitude, at two different longitudes, between January 1970 and December 1992 (Fig. 17). The data we used were derived from the Comprehensive Ocean-Atmosphere Data Set (COADS: Woodruff et al., 1987).

This analysis shows most of the Gulf Stream's interannual variability at 50 W to be at the same periods as that resulting from the simulation with a 6400 km by 4440 km basin size: the dominant peaks for the Gulf-Stream axis position, at 6 years and 20 months (Fig. 18a), agree surprisingly well, for such a simple model, with the model peaks at 6 years and 16 months. The North Atlantic simulation parameters were not specifically tuned to obtain

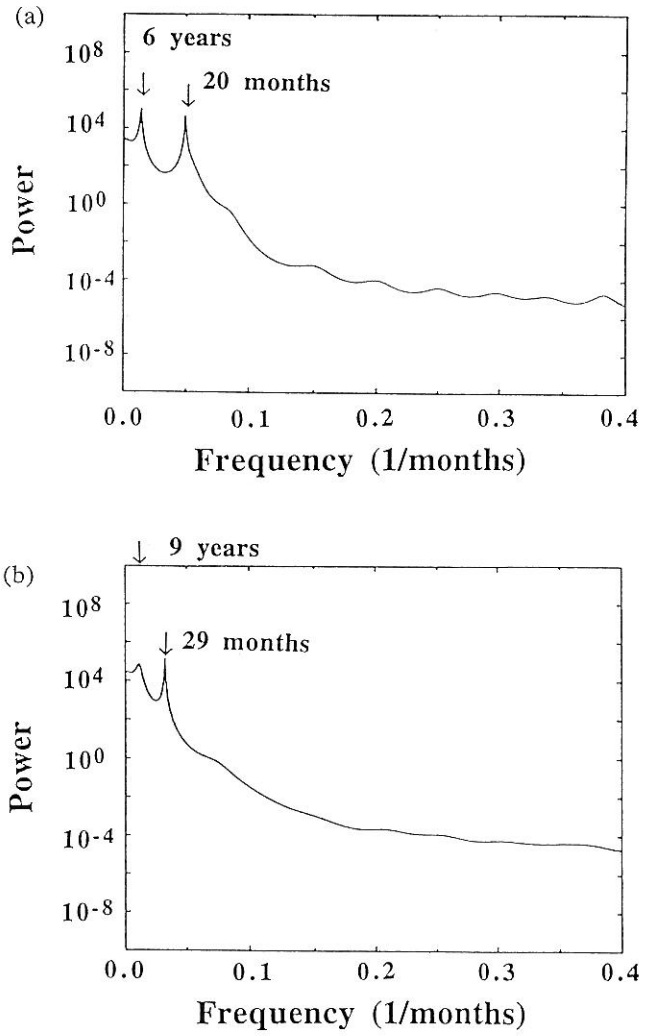

Fig. 18. Maximum-entropy spectra of the jet-axis time series from Fig. 17: *(a)* North Atlantic Ocean; *(b)* North Pacific Ocean. The time series were projected onto the first twelve SSA modes (same methodology as in Fig. 15); the order of the MEM was 20; the SSA window was 120 months (i.e., 10 years).

these results — they agree with those which had been used, prior to any observational comparison, for the complete investigation of model behavior (Table 1). Furthermore, the same peaks were found for other values of the strength of the forcing and eddy viscosity (not shown). Only the choice of H value (unchanged in all the runs) was originally made by JJG in order to have the model's barotropic Rossby wave propagation speed similar to the baroclinic speed observed in the mid-latitude ocean.

An analogous analysis for the Kuroshio axis at 146 E yields dominant peaks at 9 years and 29 months (Fig. 18b). This observational result is in qualitative agreement with the numerical results of Figs. 11 and 12, which show that the model's periods of variability increase with the width of the basin. The amplitude of the fluctuations in the Kuroshio axis also exceeds noticeably that in the Gulf Stream (compare Figs. 17a and b), in agreement with the effect of basin size on the model's oscillations in kinetic and potential energy (Figs. 11a, b). The 29-month mode detected in the northwestern Pacific cannot be attributed (Speich *et al.* 1995a) to the Quasi-Biennial (QB) oscillation known from the Equatorial Pacific (Rasmusson et al., 1990; Keppenne and Ghil, 1992; Jiang et al., 1995b): the former maintains its amplitude while the latter decays, and the former leads the latter by a few months when both are strong (not shown here).

7 Summary and Conclusions

By using techniques of numerical bifurcation theory, the multiplicity and stability of solutions to a simple, shallow-water model of the double-gyre, wind-driven ocean circulation have been determined for a rectangular mid-latitude basin, governed by Eqs. (2.1, 2.2). Multiple steady states exist in certain regions of parameter space. Circulation patterns which spontaneously break the symmetry imposed by the wind-stress forcing appear as steady stable solutions of the model for realistic values of the parameters as forcing increases, dissipation decreases, or other parameters change (Figs. 1, 2, 5, and 6).

The region where the asymmetry of the solutions manifests itself most strongly is localized near the western boundary, where the intensity of the currents is largest and so are the nonlinear effects. Indeed, as the mechanical forcing – i.e., the wind-stress magnitude – increases so does the system's nonlinearity. The strong asymmetry as well as the multiplicity of the solutions arises from the nonlinear interactions between the two recirculating cells that form near the western boundary, one in the subtropical, the other in the subpolar gyre. Initially situated near the middle of each half basin for a weak wind stress, these two cells slowly converge towards the basin's — and the forcing's — zonal symmetry axis, where they undergo stronger and stronger mutual nonlinear interactions.

Two different stable steady states emerge depending on which recirculation cell, cyclonic or anticyclonic, is more intense. It is the strongest cell that pulls water from the other across the basin's center line. These two main vorticity cells form an asymmetric dipole and entail a displacement of the confluence point north or south of the center line; consequently, the northward or southward western boundary current (WBC in the main text) overshoots when the strongest recirculating cell is the cyclonic or anticyclonic one, respectively. The solution with the opposite near-symmetry still exists, but only as an unstable steady state. The solution with the subtropical gyre dominating in extent the subpolar one seems to be stabler (Fig. 3), in agreement with the observed relative size of the two gyres in all ocean basins that possess both.

For even stronger forcing or weaker dissipation, the system's stationary solution branches undergo Hopf

bifurcation. The occurrence of such oscillatory instabilities can be also attributed to alternating nonlinear interactions between the two main cells forming the asymmetric dipole and giving rise to two smaller recirculation cells. The oscillatory dynamics of the resulting asymmetric quadrupolar structure is evident both in the linear transition patterns at the bifurcation point (Fig. 7a) and in the upper-layer thickness anomalies for a numerical experiment beyond that point (Fig. 9). By augmenting the forcing, the solutions become aperiodic as an increased number of recirculating cells interact with one another and, therefore, lead to more complex dynamics.

In the relatively limited subspace of parameters we have explored, the solutions exhibit the same qualitative behavior. Indeed, the perturbed pitchfork bifurcation and the two Hopf bifurcations – one each from the two stable steady-state branches – arise for all the parameter variations we have considered (Figs. 1, 2, 5 and 6a,b). This suggests the proximity of a pure pitchfork singularity in phase-parameter space, whose perturbation and unfolding could give rise to the behavior along the various transects we took (Golubitsky and Schaeffer, 1984).

While important thermodynamic processes and finite-amplitude effects are missing from our study, we have shown that a reduced-gravity, shallow-water, wind-driven, double-gyre model possesses a rich variety of behavior patterns, according to the values of the forcing, dissipation parameters, Rossby number, basin size, and the amplitude of the β-effect; some aspects of this behavior are quite robust We performed a set of forward integrations focused on the impact of different aspect ratios on the solutions' behavior. These showed that, for increasing basin width, the period and amplitude of the oscillations increases, and Hopf bifurcation, as well as transition to aperiodic solutions, takes place for smaller value of the wind stress σ (Figs. 11 and 12).

While our numerical study lacks realism in several respects, the results are suggestive. It is interesting to speculate on the possible relationship between the solutions obtained here with the circulation in the mid-latitude oceans. In the last 40 years there have been dramatic advances in our understanding of the western boundary layer's fundamental role in closing the circulation of the world's subtropical and subpolar gyres (Pedlosky, 1987, and references there). The nature of the currents' final separation from the western boundaries and its location, however, still give rise to considerable discussion (e.g., Ierley, 1990; Haidvogel et al., 1992). The low-frequency variability of these features suggested by our numerical study resembles, at least at a first glance, observations of the Gulf Stream, Kuroshio-Oyashio, East Australia, and Brazil and Malvinas current systems. Boland and Church (1981) reported that the East Australia Current has a point of detachment that can vary by as much as 500 km. A similar behavior for western boundary currents (WBCs in the main text) in the South Atlantic is discussed by Olson

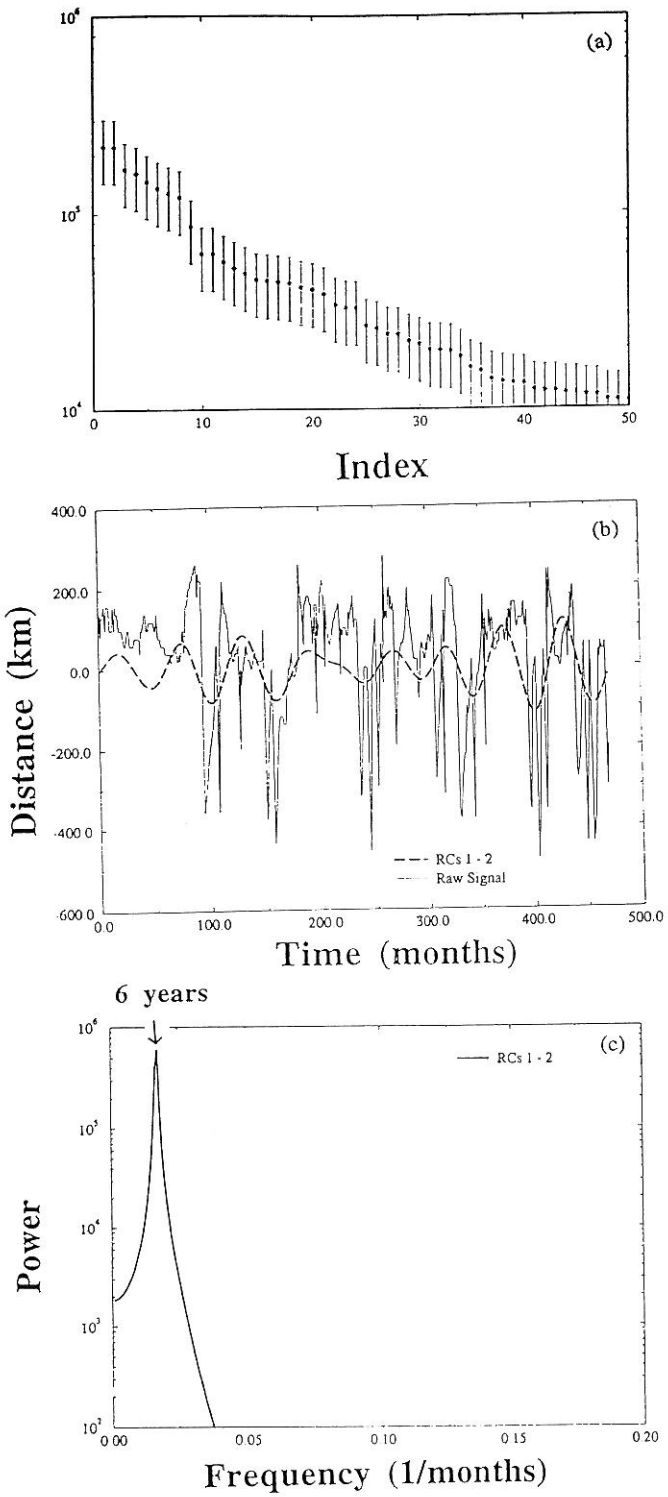

Fig. 19. Time evolution of the meridional position of the WBC confluence point for the numerical simulation of Fig. 13: *(a)* eigenvalue spectrum obtained by SSA; *(b)* the raw signal (light solid) and the time series reconstructed from the first two SSA modes (heavy dashed); and *(c)* the maximum-entropy spectrum of the first two reconstructed modes combined; MEM order and SSA window width as in Fig. 18.

et al. (1988), with the observed excursions in latitude of the separation of the Brazil and Malvinas Currents ranging over 800-1000 km. All these reported variations take place in several months.

In order to pursue the investigation in a slightly more realistic context, we performed a set of forward integrations in a rectangular domain that resembles in size the North Atlantic basin, between 20 N and 60 N. These experiments all showed strongly irregular time-dependent behavior (Figs. 13 and 14). Singular Spectrum Analysis (SSA: Vautard and Ghil, 1989; Ghil and Vautard, 1991), carried out on the time evolution of the total kinetic energy, reveals three principal modes of variability for the model in this domain: 16 months, 3.2 years, and 6 years (Fig. 15). These peaks coincide with those we obtained in examining by SSA the variability of the position of the Gulf-Stream axis (Figs. 17 and 18a).

In fact, in our North-Atlantic sized domain, the 6-year peak is directly related to the meridional fluctuations of the position of the confluence point, defined as the zero-anomaly point of the deviation of the upper-layer thickness from its value at rest 80 km east of the western wall. Indeed, the first two SSA eigenvalues for the time series of the latitudinal excursions of this point (Fig. 19a) account for the lowest-frequency variations in it (cf. the part of the signal reconstructed from these two modes and the raw signal in Fig. 19b) and their spectral peak is narrow and centered at 6 years (Fig. 19c). The order of magnitude of the meridional fluctuations of the simulated confluence point and the observed anomalies of the 15° C isotherm position in the North Atlantic are about the same (cf. Figs. 17a and 19b): the simulation gives somewhat larger fluctuations because of the model's limited vertical resolution. Plaut et al. (1995) have suggested that the non-ENSO related peak of 7-8 years in three centuries of Central England temperatures might be due to the downstream effects on the Gulf Stream extension of this 6-year peak. The spectral shift towards lower frequencies we obtained for the observed fluctuations of the 15° C isotherm position in the northwestern Pacific (Figs. 17b and 18b) goes in the same direction as our numerical results that show dominant periods increasing with increasing width of the basin (Figs. 11 and 12).

Mid-latitude ocean dynamics is, of course far more complex than revealed by the present study. Nevertheless, the preliminary agreement between the simulated and the observed North Atlantic behavior seems to support the idea that part of the double gyre's interannual variability might come from an internal mechanism like the one described here. The wind-stress forcing, of course, is not fixed in time – as assumed here – and its own seasonal and interannual variability can only add to the interest of the problem and the complexity of the observational behavior.

Appendix A: Computational Aspects of the Continuation Method

After discretization of the governing PDEs, by finite differences (as in the main text) or by spectral methods, the determination of a certain steady state is transformed into the computation of a solution to a nonlinear system of algebraic equations of the form

$$\Phi(\mathbf{u},\lambda)=0 \tag{A.1a}$$

Here $\mathbf{u}$ indicates the d-dimensional state vector and λ a particular parameter. The state vector can represent grid-point values, $\mathbf{u} = \mathbf{W}$, as for (3.1) in the main text, or spectral coefficients as in Legras and Ghil (1985). A branch γ of steady solutions $(\mathbf{u}(s), \lambda(s))$, $s_a \le s \le s_b$, is a smooth one-parameter family solutions of (A.1a). Since an extra degree of freedom is introduced by the arclength s, we need a normalization condition

$$\Sigma(\mathbf{u}(s),\lambda(s),s)=0 \tag{A.1b}$$

to close the system of equations.

A.1 Pseudo-Arclength Continuation

Geometrically, we want to determine the graph of a curve $\gamma : I \subseteq R \to R^{d+1}$, with $\gamma(s)=\left(\mathbf{u}^T(s),\lambda(s)\right)^T$, such that the equations (A.1) are satisfied. Suppose that we know, at some point s_0, a solution $(\mathbf{u}_0,\lambda_0)$ of the equation (A.1a). In many applications this is easy, since some trivial solution can always be found. The tangent to the curve $\gamma = \gamma(s)$ at $s=s_0$ is given by the vector $\dot\gamma(s_0)=\left(\dot{\mathbf{u}}^T(s_0),\dot\lambda(s_0)\right)^T$. By differentiating $\Phi(\gamma(s))=0$ with respect to s we find

$$(d\Phi)_{|\gamma(s)}\,\dot\gamma(s)\equiv\left[\Phi_{\mathbf{u}} \quad \Phi_\lambda\right]\dot\gamma(s)$$

$$=\begin{bmatrix} D_1\Phi_1 & \dots & D_d\Phi_1 & \dfrac{\partial\Phi_1}{\partial\lambda} \\ \dots & \dots & \dots & \dots \\ D_1\Phi_d & \dots & D_d\Phi_d & \dfrac{\partial\Phi_d}{\partial\lambda} \end{bmatrix}\dot\gamma(s)=0,$$

where $D_j \equiv \partial/\partial u_j$. If $(\mathbf{u}_0,\lambda_0)$ is not a bifurcation point, then $\dim\left(\ker\left(\left[\Phi_{\mathbf{u}} \quad \Phi_\lambda\right]\right)\right)=1$ and therefore $\left[\Phi_{\mathbf{u}} \quad \Phi_\lambda\right]$ has rank d. Hence we can determine $\dot\gamma(s_0)$ as the nullspace of the $d*(d+1)$ matrix $(d\Phi)_{|\gamma(s_0)}$.

First we put the matrix $\left[\Phi_{\mathbf{u}}\ \Phi_\lambda\right]$ into upper-triangular form; this is shown for $d = 3$, with x indicating nonzero elements:

$$\begin{bmatrix} x & x & x & x \\ 0 & x & x & x \\ 0 & 0 & x & x \end{bmatrix}. \tag{A.2a}$$

The last row cannot be entirely zero, and therefore the tangent $\mathbf{v}=\left(\dot{\mathbf{u}}_o^T,\dot{\lambda}_o\right)^T$ can be computed by solving

$$\begin{pmatrix} x & x & x & x \\ 0 & x & x & x \\ 0 & 0 & x & x \\ 0 & 0 & 0 & 1 \end{pmatrix}\mathbf{v}=\begin{pmatrix}0\\0\\0\\1\end{pmatrix}, \tag{A.2b}$$

with its length $\|\mathbf{v}\|$ normalized by

$$\dot{\mathbf{u}}_o^T\dot{\mathbf{u}}_o+\dot{\lambda}_o^2=1. \tag{A.2c}$$

Once $\mathbf{u}_o,\lambda_o,\dot{\mathbf{u}}_o$ and $\dot{\lambda}_o$ are determined, we can calculate a further point on the same branch by taking in (A.1b)

$$\Sigma(\mathbf{u},\lambda,s)=\dot{\mathbf{u}}_o^T(\mathbf{u}-\mathbf{u}_o)+\dot{\lambda}_o(\lambda-\lambda_o)-(s-s_o) \tag{A.1b'}$$

and solve the system (A.1) given a prescribed step length $\Delta s=s-s_o$. This form of the continuation method is called the pseudo-arclength method.

To solve the equations (A.1) we apply an Euler-predictor/Newton-corrector algorithm; let k indicate the Newton iteration index. The Euler predictor is given by

$$\mathbf{u}^1=\mathbf{u}_o+\Delta s\dot{\mathbf{u}}_o;\ \lambda^1=\lambda_o+\Delta s\dot{\lambda}_o. \tag{A.3a}$$

Once $\mathbf{u}^k$, $\dot{\mathbf{u}}^k$, λ^k and $\dot{\lambda}^k$ are calculated, the equations (A.1) are linearized about this solution, i.e.

$$\mathbf{u}^{k+1}=\mathbf{u}^k+\Delta\mathbf{u}^{k+1};\ \lambda^{k+1}=\lambda^k+\Delta\lambda^{k+1}. \tag{A.3b}$$

In every Newton iteration, this increments $\left(\Delta\mathbf{u}^{k+1},\Delta\lambda^{k+1}\right)$ are determined by solving the linear system

$$\begin{bmatrix}\Phi_{\mathbf{u}}\left(\mathbf{u}^k,\lambda^k\right) & \Phi_{\lambda}\left(\mathbf{u}^k,\lambda^k\right)\\ \dot{\mathbf{u}}_o^T & \dot{\lambda}_o\end{bmatrix}\begin{bmatrix}\Delta\mathbf{u}^{k+1}\\ \Delta\lambda^{k+1}\end{bmatrix}=\begin{bmatrix}-\Phi\left(\mathbf{u}^k,\lambda^k\right)\\ \Delta s-\dot{\mathbf{u}}_o^T\left(\mathbf{u}^k-\mathbf{u}_o\right)-\dot{\lambda}_o\left(\lambda^k-\lambda_o\right)\end{bmatrix}. \tag{A.4}$$

This linear system of equations can be solved by direct or iterative methods. In the problem of this paper, a direct solver is used since the Jacobian matrix $\Phi_{\mathbf{u}}\left(\mathbf{u}^k,\lambda^k\right)$ is ill-conditioned due to the small value of the Ekman number; the solver is based on LU decomposition (Numerical Algorithms Group, 1990).

We monitor $\det\left[\Phi_{\mathbf{u}}\left(\mathbf{u}^k,\lambda^k\right)\right]$ and $\dot{\lambda}$ along a branch to determine simple (transcritical or pitchfork) bifurcation points and turning points. Once a change in sign is found in one of these quantities between two points along a branch, say s_a and s_b, a secant process is started to locate the zero exactly. Let either function be indicated by $q(s)$; then a zero of $q(s)$ is determined by

$$s_{\ell+1}=s_\ell-q(s_\ell)\frac{s_\ell-s_{\ell-1}}{q(s_\ell)-q(s_{\ell-1})}, \tag{A.5a}$$

$$s_0=s_a,\ s_1=s_b. \tag{A.5b,c}$$

The stopping criterion for the iteration is $|s_{\ell+1}-s_\ell|/s_a<\varepsilon$, where $\varepsilon=10^{-3}$. In some cases, a larger ε must be taken because the matrix $\Phi_{\mathbf{u}}$ becomes too singular. We check *a posteriori* that the value of $q(s)$ is substantially smaller than the values at both s_a and s_b.

A.2. Eigenproblem Solver

If $\det\left[\Phi_{\mathbf{u}}\left(\mathbf{u}^k,\lambda^k\right)\right]$ changes sign but $\dot{\lambda}$ does not, a simple bifurcation point is detected and a branch switch process is started. Let $\hat{\Phi}_{\mathbf{u}}=\Phi_{\mathbf{u}}\left(\mathbf{u}_*,\lambda_*\right)$ be the Jacobian matrix at the bifurcation point $\left(\mathbf{u}_*,\lambda_*\right)$ just after the secant iteration has converged. Further let the tangent along the already known branch at $s=s_a$ be indicated by $\left(\dot{\mathbf{u}}_o^T,\dot{\lambda}_o\right)^T$. First we calculate the nullvector ϕ of $\hat{\Phi}_{\mathbf{u}}$ by inverse iteration and construct a vector $\left(\hat{\mathbf{u}}^T,\hat{\lambda}\right)^T$ orthogonal to $\left(\dot{\mathbf{u}}_o^T,\dot{\lambda}_o\right)^T$ by solving

$$\begin{bmatrix}\hat{\Phi}_{\mathbf{u}} & \hat{\Phi}_{\lambda}\\ \dot{\mathbf{u}}_o^T & \dot{\lambda}_o\end{bmatrix}\begin{bmatrix}\hat{\mathbf{u}}\\ \hat{\lambda}\end{bmatrix}=\begin{bmatrix}\mathbf{0}\\0\end{bmatrix}, \tag{A.6a}$$

where $\hat{\mathbf{u}}$ is easily expressed in terms of ϕ. To determine a point on the new branch, the Newton process is started with the Euler predictor

$$\mathbf{u}^1=\mathbf{u}_*\pm\Delta s\hat{\mathbf{u}},\qquad \lambda^1=\lambda_*\pm\Delta s\hat{\lambda}. \tag{A.6b}$$

The $\pm$ indicates that points can be found on either side of the known branch. When a point on a new branch has been located, the pseudo-arclength procedure is used to compute further points.

There is no simple indicator for Hopf bifurcations. The linear stability problem of steady states along the branch has to be solved to detect these bifurcations. When this problem is discretized, a generalized eigenvalue problem of the form

$$\mathcal{A}x=\eta\mathcal{B}x \tag{A.7}$$

appears, with $\mathcal{A}\equiv\Phi_{\mathbf{u}}(\mathbf{u},\lambda)$ and $\mathcal{B}$ a singular diagonal matrix. A complex mapping of the form

$$\eta=b+a\frac{\kappa-1}{\kappa+1} \tag{A.8}$$

is applied, with b real and a positive; it transforms the eigenvalue problem into

$$\mathcal{E}\mathbf{x}=\mathcal{D}^{-1}C\mathbf{x}=\kappa\mathbf{x} \tag{A.9}$$

where $C=\mathcal{A}+(a-b)\mathcal{B}$ and $\mathcal{D}=-\mathcal{A}+(a+b)\mathcal{B}$. By the mapping (A.8), the most dangerous modes of the original problem (A.7), i.e., those closest to the imaginary axis, are

mapped onto the dominant modes of the problem (A.9), i.e., those with largest norm. Writing $\eta - b = x + iy$ and $\kappa = \kappa_1 + i\kappa_2$ gives the relations

$$\kappa_1 = \frac{a^2 - x^2 - y^2}{(x-a)^2 + y^2}, \quad \kappa_2 = \frac{2ay}{(x-a)^2 + y^2}. \tag{A.10}$$

The simultaneous iteration procedure (SIT) is applied to the problem (A.9). We start with m initial vectors $\mathbf{U}_j$, $j = 1,\ldots, m$ and use the notation

$$\mathcal{U}^0 = [\mathbf{U}_1,\ldots,\mathbf{U}_m] \tag{A.11a}$$

During the filtering stage of the SIT, we compute for $n = 1,\ldots, N$ the product

$$\mathcal{U}^n = \mathcal{E}\mathcal{U}^{n-1} \tag{A.11b}$$

by solving the linear systems

$$\mathcal{D}\mathcal{U}^n = C\mathcal{U}^{n-1}, \tag{A.11c}$$

Let Λ denote the diagonal matrix with eigenvalues ordered according to their norm and Q the corresponding eigenvectors, i.e.

$$\Lambda = \begin{bmatrix} \kappa_1 & 0 & 0 \\ 0 & \ldots & 0 \\ 0 & 0 & \kappa_d \end{bmatrix}, \quad Q = [\mathbf{q}_1,\ldots,\mathbf{q}_d] \tag{A.12}$$

with $\mathcal{E}\mathbf{q}_i = \mu_i \mathbf{q}_i$. The idea is to decompose

$$\mathcal{U} = \mathcal{U}^0 = Q_a C_a + Q_b C_b \tag{A.13a}$$

so that the $(d*m)$ matrix Q_a contain the first m columns of Q and Q_b the remainder of the columns of Q. After one step (A.11c) we obtain

$$\mathcal{V} = \mathcal{U}^1 = \mathrm{E}(Q_a C_a + Q_b C_b) = Q_a \Lambda_a C_a + Q_b \Lambda_b C_b, \tag{A.13b}$$

where Λ_a is the $(d*m)$ matrix of the first m columns of Λ. Hence, after each filtering step, the components of the starting vectors in the direction of the dominant eigenvectors increase most in amplitude.

After a certain number of filtering steps N, usually 5 to 10, a reorientation step is performed to obtain a better approximation to the eigensolution of (A.9). First, we compute the $m * m$ matrices

$$\mathcal{F} = \mathcal{U}^T\mathcal{U}, \quad \mathcal{G} = \mathcal{U}^T\mathcal{V} \tag{A.14a}$$

and solve for the matrix $\mathcal{H} = \mathcal{G}^{-1}\mathcal{F}$ from

$$\mathcal{F}\mathcal{H} = \mathcal{G}. \tag{A.14b}$$

The eigenvalues of the matrix H are an approximation of the eigenvalues of E, since

$$\begin{aligned} \mathcal{F}\mathcal{H} &= \mathcal{U}^T\mathcal{U}\mathcal{H} = \mathcal{U}^T(Q_a C_a + Q_b C_b)\mathcal{H} = \mathcal{G} \\ &= \mathcal{U}^T\mathcal{V} = \mathcal{U}^T(Q_a \Lambda_a C_a + Q_b \Lambda_b C_b). \end{aligned} \tag{A.15}$$

Because $\mathcal{U}^T Q_a$ is nonsingular, we obtain — by omitting the part associated with Λ_b from (A.15) —

$$C_a\mathcal{H} = \Lambda_a C_a. \tag{A.16a}$$

In the actual numerical code, we solve the eigenvalue problem

$$\mathcal{H}\mathcal{P} = \mathcal{P}\Lambda_a \tag{A.16b}$$

to yield $\mathcal{P} = C_a^{-1}$ and compute

$$\mathcal{W} = \mathcal{V}\mathcal{P} = Q_a\Lambda_a + Q_b\Lambda_b C_b C_a^{-1}. \tag{A.16c}$$

The next approximation to the eigenvectors is then found from the first m columns of the matrix W.

The accuracy of the approximation of the eigensolution after the p-th reorientation is determined by backsubstituting the eigenvalues and eigenvectors into the original eigenvalue problem (A.9), computing the residue and dividing it by the L_2-norm of the corresponding eigenvector. The stopping criterion is that this residue is smaller than some prescribed quantity, usually 10^{-3}. In most cases, this process converges within P reorientations. When converged, the eigenvalues of the original problem are computed by the complex mapping (A.8).

A.3. Summary of the Complete Algorithm

The complete algorithm that combines the continuation method with the eigenproblem solver can now be summarized as follows. Suppose a point $(\mathbf{u}_0, \lambda_0)$ on a given branch of stationary solutions, the tangent $(\dot{\mathbf{u}}_0, \dot{\lambda}_0)$ to the branch at that point and m eigenvectors (and eigenvalues $\eta_1,\ldots, \eta_m$) of the linearization of (3.1) about that point have been computed.

1. Compute the next Euler-forward guess: $\mathbf{u} = \mathbf{u}_0 + \Delta s\dot{\mathbf{u}}_0$, $\lambda = \lambda_0 + \Delta s\dot{\lambda}_0$.
2. Compute the Jacobian $\mathbf{\Phi}_\mathbf{u}$ and solve the system (3.1, 3.3) by Newton iteration with the initial guess given by step 1, until convergence to within the present ε in K steps, say. This requires the solution of $2K$ systems of linear equations.
3. Compute the matrix $\mathcal{D}$ in (A.9) and start the SIT with the m starting (eigen)vectors. With filtering index $1 \le n \le N$ and P reorientations until convergence, this requires the solution of $m\,N\,P$ linear systems.
4. Compute a desired number of test functions, for example $\det(\mathbf{\Phi}_\mathbf{u})$, and initiate computation of a new solution branch, if called for by the result of a test.

The linear systems are all solved by direct LU decomposition, taking into account of the banded structure of the Jacobian (Numerical Algorithms Group 1990).

Acknowledgments. It is a pleasure to thank Shi Jiang for many useful discussions and numerous colleagues for data, preprints and comments; discussions with Kayo Ide were particularly fruitful. The authors are indebted to the anonymous referees for helpful comments and suggestions. This work was supported by a NOAA Climate and Global Change Post-Doctoral Fellowship (SS), and by an NSF Special Creativity Award (MG). HD thanks J. David Neelin for support (NSF grant ATM-9158294) of a visit to UCLA during which the collaboration leading to this paper was initiated. MG also thanks the Ecole Normale Supérieure for the Condorcet Visiting Chair, whose support helped complete the revision of the paper. The computing resources were provided by the *Centre de Calcul pour la Recherche* of the Université Pierre et Marie Curie, Paris, and by NCAR's Scientific Computing Division.

References

Auer, S. J., Five-year climatological survey of the Gulf Stream system and its associated rings. *J. Geophys. Res., 92*, 11726-11790, 1987.

Boland, F. M. and Church, J. A., The East Australian Current 1978. *Deep-Sea Res., 28A*, 937-957, 1981.

Broomhead, D. S. and King, G. P., Extracting qualitative dynamics from experimental data. *Physica, 20D*, 217-236,1986.

Brown, O. B. and Evans, R. H., Satellite infrared remote sensing. In *Study of Physical Processes on the U.S. Mid-Atlantic Slope and Rise.* Casagrande (ed.), Science Applications International, Raileigh, NC, *IV*, 67- 97,1987.

Bryan, F., High-latitude salinity effects and interhemispheric thermohaline circulation. *Nature, 3é3*, 301-304, 1986.

Bryan, K., A numerical investigation of a non-linear model of a wind-driven ocean. *J. Atmos. Sci., 20*, 549-606, 1963.

Cessi, P. and Ierley, G. R., Symmetry-breaking multiple equilibria in quasi-geostrophic, wind-driven flows. *J. Phys. Oceanogr., 25*, 1196-1205, 1995.

Cessi, P. and Thompson, L., Geometrical control of inertial recirculation. *J. Phys. Oceanogr., 20*, 1867-1875, 1990.

Cessi, P., Ierley,G., and Young, W., A model of the inertial recirculation driven by potential vorticity anomalies. *J. Phys. Oceanogr., 17*, 1640-1652,1987.

Charney, J. G. and DeVore, J. G., Multiple flow equilibria in the atmosphere and blocking. *J. Atmos. Sci., 36*, 1205-1216, 1979.

Christodoulou, K. N. and Scriven, L. E., Finding leading modes of a viscous free surface flow: An asymmetric generalized eigenproblem. *J. Sci. Comput., 3*, 355-406, 1988.

Colebrook, J. M., Continuous plankton records: zooplankton and environment, Northeast Atlantic and North Sea, 1948-1975, *Oceanol. Acta, 1*, 9-23, 1978.

Constantin, P., Foias, C., Nicolaenko, B., and Témam,R. , *Integral Manifolds and Inertial Manifolds for Dissipative Partial Differential Equations*, Springer-Verlag, New York, 122 pp., 1989.

Dijkstra, H. A., On the structure of cellular solutions in Rayleigh-Bénard-Marangoni flows in small-aspect-ratio containers, *J. Fluid Mech., 243*, 73-102, 1992.

Dijkstra, H. A. and Neelin, J. D., On the attractors of an intermediate coupled ocean-atmosphere model. *Dyn. Atmos. Oceans*, 22,19-48, 1995.

Fedorov, K. N., Ginsburg, A. I., and Kostianoy, A. G., Modelling of "mushroom-like" currents (vortex dipoles) in a laboratory tank with rotating homogeneous and stratified fluids. In: *Mesoscale/Synoptic Coherent Structures in Geophysical Turbulence*. J. C. J. Nihoul (ed.), Elsevier, 840 pp., 1989.

Flierl, G. R., Larichev, V. D., McWilliams, J. C., and Reznik, G. M., The dynamics of baroclinic and barotropic solitary eddies. *Dyn. Atmos. Oceans, 5*, 1-41, 1980.

Flierl, G. R., Stern, M. E., and Whitehead, J. A., The physical significance of modons: Laboratory experiments and general integral constraints. *Dyn. Atmos. Oceans, 7*, 233-263, 1983.

Fraedrich, K., Estimating the dimensions of weather and climate attractors. *J. Atmos. Sci., 43*,419-432, 1986.

Fu, L.-L., Christensen, E. J., Yamarone, C. A., Lefebvre, M., Ménard, Y., Dorrer, M., and Escudier, P., TOPEX/POSEIDON mission overview. *J. Geophys. Res., 99*, 24369-24382, 1994.

Ghil, M. and Childress, S., *Topics in Geophysical Fluid Dynamics: Atmospheric Dynamics, Dynamo Theory and Climate Dynamics*, Springer-Verlag, New York, 485 pp, 1987.

Ghil, M. and Tavantzis, J., Global Hopf bifurcation in a simple climate model. *SIAM J. Appl. Math., 43*, 1019-1041, 1983.

Ghil, M. and Vautard, R., Interdecadal oscillations and the warming trend in the global temperature series. *Nature, 350*, 324-327, 1991.

Golub, G. H. and Van Loan, C. F., *Matrix Computations* (2nd ed.), The Johns Hopkins University Press, Baltimore and London, 642 pp, 1989.

Golubitsky, M. and Schaeffer, D. G., *Singularities and Groups in Bifurcation Theory*, Springer-Verlag, New York, 463 pp.

Guckenheimer J., and P. Holmes, 1983: *Nonlinear Oscillations, Dynamical Systems, and Bifurcations of Vector Fields*, Springer-Verlag, *459* pp, 1984.

Haidvogel, D. B., McWilliams, J. C., and Gent, P. R., Boundary current separation in a quasigeostrophic, eddy-resolving ocean circulation model. *J. Phys. Oceanogr., 22*, 882-902, 1992.

Hanson, H. P., Climatological perspectives, oceanographic and meteorological, on variability in the subtropical convergence zone in the Northwestern Atlantic. *J. Geophys. Res., 96*, 8517-8529, 1991.

Holland, W. R., The role of mesoscales eddies in the general circulation of the ocean-numerical experiments using a wind-driven quasi-geostrophic model. *J. Phys. Oceanogr., 8*, 363-392, 1978.

Holland, W. R. and Lin, L. B., On the generation of mesoscale eddies and their contribution to the oceanic general circulation. I. A preliminary numerical experiment. *J. Phys. Oceanogr., 5*, 642-656, 1975.

Ierley, G. R., Boundary layers in the general ocean circulation. *Annu. Rev. Fluid Mech., 22*, 111-142, 1990.

Ierley, G. and Young, W., Inertial recirculation in a β-plane corner. *J. Phys. Oceanogr., 18*, 683-689, 1988.

Jiang, S., *Data Assimilation for a Nonlinear, Wind-Driven, Shallow-Water Model in a Rectangular Midlatitude Basin.* Ph.D. thesis, University of California, Los Angeles, 247 pp, 1994.

Jiang, S., Jin, F.-F., and Ghil, M., Multiple equilibria, periodic and aperiodic solutions in a wind-driven, double-gyre, shallow-water model. *J. Phys. Oceanogr., 25*, 764-786, 1995a.

Jiang, N., Neelin, J. D., and Ghil, M., Quasi-quadriennial and quasi-biennial variability in equatorial Pacific sea surface temperatures and winds. *Clim. Dyn.*, accepted, 1995b.

Jin, F.-F. and Ghil, M., Intraseasonal oscillations in the extratropics: Hopf bifurcation and topographic instabilities. *J. Atmos. Sci.*, *47*, 3007-3022, 1990.

Jin, F.-F., Neelin, J. D., and Ghil, M., El Niño on the Devil's Staircase: Annual subharmonic steps to chaos. *Science*, *264*, 70-72, 1994.

Keller, H. B., Numerical solution of bifurcation and nonlinear eigenvalue problems. In *Applications of Bifurcation Theory* (ed. P. H. Rabinowitz), Academic Press, 1977.

Keppenne, C. L., *Bifurcations, Strange Attractors and Low-Frequency Dynamics*. Ph.D. thesis, Université Catholique de Louvain, Louvain-la-Neuve, Belgium, 159 pp, 1989.

Keppenne, C. L. and Ghil, M., Adaptive filtering and prediction of the Southern Oscillation Index. *J. Geophys. Res.*, *97*, 20449-20454, 1992.

Kimoto, M. and Ghil, M., Multiple flow regimes in the Northern Hemisphere winter. Part I: Methodology and hemispheric regimes. *J. Atmos. Sci.*, *50*, 2625-2644, 1992a.

Kimoto, M. and Ghil, M., Multiple flow regimes in the Northern Hemisphere winter. Part II: Sectorial regimes and preferred transitions. *J. Atmos. Sci.*, *50*, 2645-2673, 1992b.

Legras, B., Eddies in geophysical flows. In: *Geophysical Fluid Dynamics*, Summer School, Roscoff, France. INSU - CNRS - METEO-France - IFREMER - CNES, 228 pp, 1992.

Legras, B. and Ghil, M., Persistent anomalies, blocking, and variations in atmospheric predictability. *J. Atmos. Sci.*, *42*, 433-471, 1985.

Le Provost, C. and Verron, J., Wind-driven ocean circulation transition to barotropic instability. *Dyn. Atmos. Oceans*, *11*, 175-201, 1987.

Levitus, S., Interpentadal variability of steric sea level and geopotential thickness of the North Atlantic ocean, 1970-1974 versus 1955-1959. *J. Geophys. Res.*, *95*, 5233-5238, 1990.

Lorenz, E. N., Deterministic nonperiodic flow. *J. Atmos. Sci.*, *20*, 130-141, 1963.

Lorenz, E. N., Can chaos and intransitivity lead to interannual variability? *Tellus*, *42A*, 378-389, 1990.

McCalpin, J. and Haidvogel, D. B., Phenomenology of the low-frequency variability in a reduced-gravity, quasigeostrophic double-gyre model. *J. Phys. Oceanogr.*, submitted, 1995.

McWilliams, J.C., N.J. Norton, P.R. Gent, and D.B. Haidvogel, A linear balance model of wind-driven, mid-latitude ocean circulation. *J. Phys. Oceanogr.*, *20*, 1349-1378, 1990.

Moro, B., On the non-linear Munk model. II: Stability. *Dyn. Atmos. Oceans*, *14*, 203-227, 1990.

Neelin, D. J., Latif, M., Allaart, M. A. F., Cane, M. A., Cubash, U., Gates, W. L., Gent, P. R., Ghil, M., Gordon, C., Lau, N. C., Mechoso, C. R., Meehl, G. A., Oberhuber, J. M., Philander, S. G. H., Schopf, P. S., Sperber, K. R., Tokioka, T., Tribbia, J., and Zebiak, S., Tropical air-sea interaction in general circulation models. *Clim. Dyn.*, *7*, 73-104, 1992.

Nguyen Duc, J.-M. and Sommeria, J., Experimental characterization of steady two-dimensional vortex couples. *J. Fluid Mech.*, *192*, 175-192, 1988.

North, G. R., Cahalan, R. F., and Coakley, Jr., J. A., Energy balance climate models. *Rev. Geophys. Space Phys.*, *19*, 91-121, 1981.

Numerical Algorithms Group, *NAG Fortran Library Manual, MARK 14*. Numerical Algorithms Group, Inc., Oxford, UK, 1990.

Olson, D. B., Podestà, G. P., Evans, R. H., and Brown, O. B., Temporal variations in the separation of Brazil and Malvinas Currents. *Deep-Sea Res.*, *35*, 1971-1990, 1988.

Pedlosky, J., *Geophysical Fluid Dynamics* (2nd ed.), Springer-Verlag, New York/Heidelberg/Berlin, 710 pp., 1987.

Philander, S. G. H., *El Niño, la Niña, and the Southern Oscillation*, Academic Press, San Diego, 293 pp., 1990.

Plaut, G., Ghil, M., and Vautard, R., Interannual and interdecadal variability in 335 years of Central England temperature. *Science*, *268*, 710-713, 1995.

Qiu, B. and Joyce, T. M., Interannual variability in the mid- and low-latitude western North Pacific. *J. Phys. Oceanogr.*, *22*, 1062-1079, 1992.

Quon, C. and Ghil, M., Multiple equilibria in thermosolutal convection due to salt-flux boundary conditions. *J. Fluid Mech.*, *245*, 449-483, 1992.

Quon, C. and Ghil, M., Multiple equilibria and stable oscillations in thermosolutal convection at small aspect ratio. *J. Fluid Mech.*, *291*, 33-56, 1995.

Rasmusson, E. M., Wang, X., and Ropelewski, C. F., The biennial component of ENSO variability. *J. Mar. Systems*, *1*, 71-96, 1990.

Robinson, A. R. (ed.), *Eddies in Marine Science*. Springer-Verlag, 609 pp., 1983.

Seydel, R., *From Equilibrium to Chaos. Practical Bifurcation and Stability Analysis*. Elsevier, 367 pp., 1988.

Speich, S. and Ghil, M., Interannual variability of the mid-latitude oceans: A new source of climate variability? *Sistema Terra*, *3*, 33-35, 1994.

Speich, S., Ghil, M., and Dijkstra, H., Low-frequency variability of western boundary currents: Numerical experiments and observational evidence. In: *Proceedings of the First Institute on Global Climate Change*, NOAA-UCAR, Boulder, CO. In press, 1995a.

Speich, S., Madec, G., and Crépon, M., A process study of a strait outflow circulation: The case of the Alboran Sea. *J. Phys. Oceanogr.*, in press, 1995b.

Steward, W. J. and Jennings, A., A simultaneous iteration algorithm for real matrices. *ACM Trans. Math. Software*, *7*, 184-198, 1981.

Stommel,H., Thermohaline convection with two stable regimes of flow. *Tellus*, *13*, 224-228, 1961.

Strong, C., Jin, F.-F., and Ghil, M., Intraseasonal oscillations in a barotropic model with annual cycle, and their predictability. J. Atmos. Sci., in press, 1995.

Témam, R., *Infinite-Dimensional Dynamical Systems in Mechanics and Physics*, Springer-Verlag, New York, 500 pp., 1988.

Thual, O. and McWilliams, J. C., The catastrophe structure of thermohaline convection in a two-dimensional fluid model and a comparison with low-order box model. *Geophys. Astrophys. Fluid Dyn.*, *64*, 67-95, 1992.

Van Heijst, G. J. F. and Flor, J. B., Laboratory experiments on dipole structures in a stratified fluid. In: *Mesoscale/Synoptic Coherent Structures in Geophysical Turbulence*, J. C. J. Nihoul (ed.), Elsevier, 841 pp., 1989.

Vautard, R. and Ghil, M., Singular spectrum analysis in nonlinear dynamics, with applications to paleoclimatic time series. *Physica*, *D35*, 395-424, 1989.

Vautard, R., Yiou, P., and Ghil, M., Singular Spectrum Analysis: A toolkit for short, noisy, chaotic signals. *Physica* , *D58*, 95-126, 1992.

Veronis, G., Wind-driven ocean circulation. Part I: Linear theory and perturbation analysis. *Deep-Sea Res.*, *13*, 17-29, 1966a.

Veronis, G., Wind-driven ocean circulation. Part II: Numerical solutions of the nonlinear problem. *Deep-Sea Res.*, *13*, 31-55, 1966b.

Verron, J. and Blayo, E., The no-slip condition and the Gulf Stream separation problem. *J. Phys. Oceanogr.*, submitted, 1995.

Verron, J. and Jo, J.-H., On the stability of wind-driven barotropic ocean circulations. *Fluid Dyn. Res.*, *14*, 7-27, 1994.

Verron, J. and Le Provost, C., Response of eddy-resolved general circulation models to asymmetrical wind forcing. *Dyn. Atmos. Oceans*, *15*, 79-93, 1991.

Weaver, A. J., Sarachik, E. S., and Marotzke, J., Freshwater flux forcing of decadal and interdecadal oceanic variability. *Nature*, *353*, 836-838, 1991.

Woodruff, S. D., Slutz, R. J., Jenne, R. L., and Steurer, P. M., A comprehensive ocean-atmosphere data set, *Bull. Amer. Met. Soc.*, *68*, 521-527, 1987.